CU_CUPG-01_PTD Technical Specification – Annex No. 4

KEY SIMULATIONS RESULTS

REV. 2/2023

TABLE OF CONTENTS

1. INTRODUCTION

This document provides a general overview of the key expected load scenarios of the Vacuum vessel in the COMPASS-U tokamak, presents the results of electromagnetic, heating, and structural simulations performed by the IPP (the Buyer).

The results presented do by no means reflect all analyses that have been explored and performed, but they cover the key scenarios and areas of interest of the Vacuum vessel. Information and conclusions contained in this document may help to the Seller to understand under what operating conditions the VV will be run in the tokamak. They also bring supporting arguments and reasoning of the design of the individual areas of the VV.

The Seller is not expected to perform his own analyses regarding operation regimes and further elaborate on any individual scenarios. Information contained in this document serves for informative purposes and should round up the whole technical assignment.

2. EXPECTED OPERATION AND LOAD SCENARIOS OVERVIEW

2.1. Selection of the disruption events parameters

In the following paragraphs, an engineering effort to find the worst possible electromagnetic load which the vacuum vessel of the COMPASS-U tokamak might be subjected to during its lifetime is described. The parameters of the disruption events and sequences are selected as the maximal ones and provide an upper bound of disruption loads that was considered in the mechanical design of the vacuum vessel. The considered disruption loads include 4 particular phenomena: current quench (CQ), vertical displacement events (VDE), quench of toroidal magnetic flux (QTF) and halo currents.

2.1.1. Current quench (CQ) rate

Data from other tokamaks show that current quench time ranges from milliseconds for rather small machines to hundreds of milliseconds in case of the large ones. Even for the same machine, it might differ several times depending on the particular discharge. In order to find the fastest possible current quench rate providing the largest induced currents in the passive conductive structures, scaling based on the Wesley's dataset (Figure 1) was considered. It predicts value up to 3.29 MA/ms for COMPASS-U parameters (for normalized internal inductance l_i = 0.4 H/m, elongation κ = 1.8).

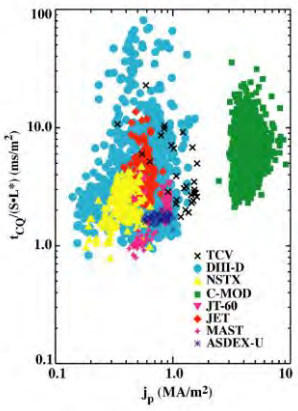

Figure 1: Wesley's dataset [1].

Scaling based on an alternative Hender's dataset (Figure 2) predicts current quench rate value about 2.7 MA/ms. As a result, a value of 3 MA/ms of current quench is considered in the FE calculations for COMPASS-U tokamak.

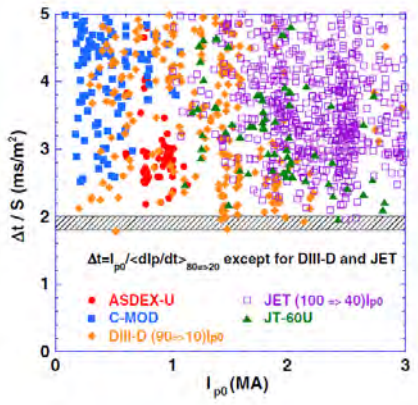

Figure 2: Hender's dataset [2].

2.1.2. Vertical displacement events (VDE)

In order to find the largest possible forces on the VV and PSP, several positions where plasma column may appear after its either vertical or radial movement from the central position, were identified as it is illustrated in the Figure 3.

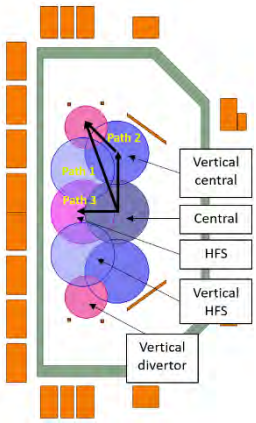

Figure 3: Positions of the plasma column after its movement which are considered in the FE analysis.

It was proposed that plasma may get into these positions with some maximal value of the toroidal current which respects only decrease from the initial 2 MA to maintain radial force balance. Table 1 presents the maximal currents and minor radii of plasma column at the positions of interest.

Table 1: Plasma parameters at different positions considered in the VDE analysis.

Position	*R* [m]	*Z* [m]	*a* [m]	I_P [MA]
Central	0.894	0.0	0.15	2.0
HFS	0.734	0.0	0.15	1.6
Vertical central	0.894	±0.279	0.15	2.0
Vertical divertor	0.75	±0.4	0.1	1.7

Two different trajectories of the plasma column during vertical displacement events are proposed: path no. 1 of fast VDEs towards divertor, which might be triggered e.g. by sudden drop of kinetic plasma pressure, which might shift the plasma column out of the vertically stable position, and path no. 2 of slow VDEs driven by time constant of PSP which might be caused e.g. by failure of the vertical stabilization system. To satisfy the force-free condition on the plasma column during plasma movement, VDE rate was tuned in such a way that the attractive vertical force from the PF coils is compensated by the repulsive force from eddy currents induced in the conductive parts which plasma approaches. The left graph in the Figure 4 shows how the attractive force on the plasma column from PF coils changes along the path no. 1 for different equilibria. The maximum is 5.68 MN for DHSF' equilibrium (plasma moves upwards) in the vertical divertor position of the plasma. If plasma gets from the central position to the vertical divertor position in 1.55 ms, this force is exactly compensated by the repulsive force of the induced eddy currents (black circle in the right graph in the Figure 4). Similar analysis was done for path no. 2 – time interval for plasma to get from central position to the vertical central one is 35 ms in this case. Then, plasma moves in 0.1 ms to the vertical divertor position.

Radial disruptions are resolved along the path no. 3 in the Figure 3 where plasma moves in 1 ms from the central to the HFS position.

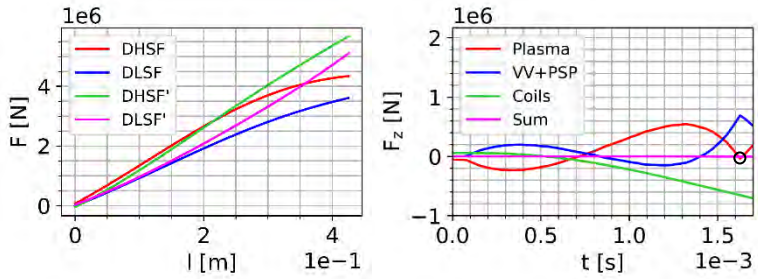

Figure 4. Left: Attractive vertical force on the plasma column from the PF coils along the path no. 1 from central to vertical divertor position for different equilibria. Right: Balance of vertical force between plasma column, PF and CS coils and induced eddy currents in the VV and PSP. Plasma movement in 1.55 ms along the path no. 1 is accompanied by decrease of plasma current from 2 MA to 1.7 MA and decrease of minor radius from 0.15 m to 0.1 m.

2.1.3. Quench of the toroidal magnetic flux (QTF)

Classical equation

$$\Delta\phi_{par} = \frac{\mu_0^2}{8\pi}\frac{I_P^2}{B_T}$$

provides an upper estimate of paramagnetic flux caused by the poloidal plasma current. For the COMPASS-U parameters (I_P = 2 MA, B_T = 5 T) it gives value of 50 mWb which is further used for FE modelling of quench of the toroidal magnetic flux during current quench (QTF CQ).

Modelling of the foreseen COMPASS-U plasma scenarios by means of FIESTA [3] and METIS [4] codes provides an upper bound of plasma thermal energy about W_T = 830 kJ for a discharge with 18 MW of heating power which is the maximal value available in the later operational phases. According to the expression

$$\Delta\phi_{dia} = -\frac{2}{3}\frac{\mu_0}{B_T}\frac{W_T}{2\pi R}$$

value about –25 mWb of diamagnetic flux caused by thermal plasma energy is obtained. An alternative equation [5]

$$\Delta\phi_{pl} = \frac{2\kappa}{\kappa^2+1}\frac{\mu_0^2}{8\pi}\frac{I_P^2}{B_T}(1-\beta_P)$$

predicts diamagnetic flux about –32 mWb for $\beta_P = 0.65$. As a safe upper bound, value -35 mWb is used for modelling of quench of the toroidal magnetic flux caused by thermal quench (QTF TQ). According to the data from other tokamaks (Figure 5), t_{TQ} = 0.1 ms can be well used as a safe lower bound of the TQ duration.

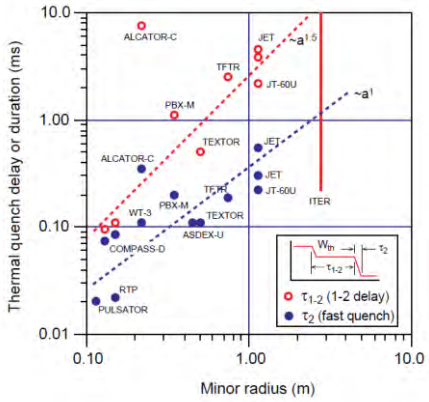

Figure 5: Thermal quench times [6].

2.1.4. Halo currents

According to the ITPA disruption database [6] (see Figure 6) which gathers halo current data from the most of the tokamaks, product of halo fraction *F* and toroidal peaking factor *TPF* can be bounded by constant $F \times TPF = 0.75$. For $TPF = 1$ (symmetrical disruptions), it means that the total halo current I_H might reach up to 75% of the pre-disruptive plasma current I_P. Halo currents start to originate when plasma approaches the first wall structures. In the FE model, halo currents are triggered when plasma reaches its final position during the movement and CQ starts. Figure 7 presents the considered halo current paths for the particular plasma positions and time profile of the halo current which is tied to the time profile of the plasma current during CQ.

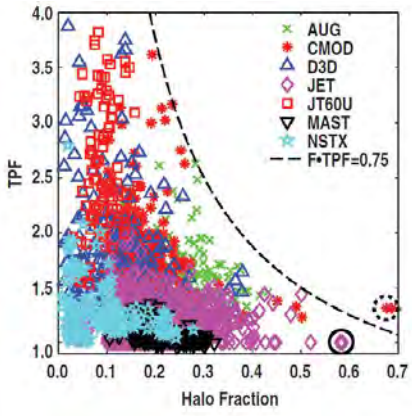

Figure 6: Toroidal peaking factor versus halo fraction [6].

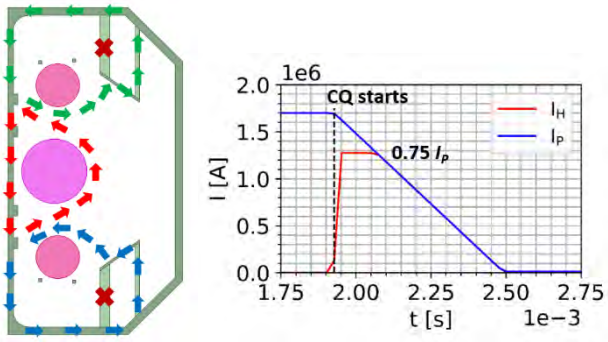

Figure 7: Halo current paths considered in the FE model and time profile of the halo current I_H dependent on plasma current I_P.

2.1.5. Plasma equilibria

Out of a set of 13 representative plasma equilibria (including circular, elongated and D-shaped plasma) which were obtained by FIESTA [3] code and which are foreseen as the operational space of the COMPASS-U, two were selected for the further disruption analysis as those which well represent maximal possible poloidal magnetic field along the VV shell. The selected equilibria are for D-shaped plasma of high/low triangularity with high X-point (marked as DHSF and DLSF respectively), see Figure 8. As the design requirement for the VV assumes installation of both top and bottom divertor, versions flipped over the midplane of the two selected equilibria are also considered (marked as DHSF' and DLSF').

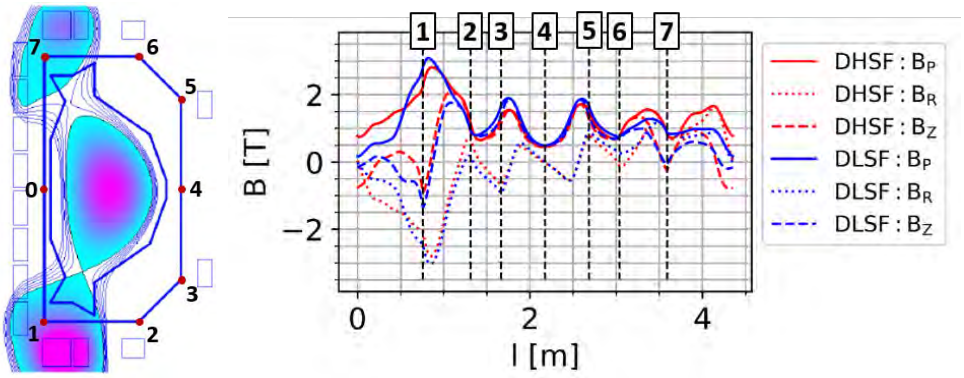

Figure 8: Poloidal magnetic field of the plasma equilibria selected for the disruption calculations along the VV shell (full line – magnitude, dotted line – radial component, dashed line – vertical component). Figure in the left depicts DHSF plasma equilibrium.

2.2. List of the considered critical disruption sequences

Phenomena described in the previous subsection usually appear in a certain time sequence during the disruption event. All of the disruption sequences that are proposed for FE modelling can be divided into 4 groups according to the way of plasma movement (Table 2). The group no. 1 represents quench of plasma current at major radius without any movement of the plasma column, group no. 2 radial disruptions towards HFS part of the VV and group no. 4 and 5 vertical displacement events to divertor (fast and slow respectively). Each of the groups contains several variants of disruption sequences differing in the type of equilibria applied and in the direction of the disruption event (upwards/downwards in the case of groups no. 4 and 5).

Table 2: List of the critical disruption sequences

No.	Spec.	Disruption sequence
Group 1: Major disruption (no plasma movement)		
1.1	DHSF	CQ + QTF CQ
1.2	DLSF	
Group 2: Radial disruptions (1ms movement to HFS position)		
2.1	DHSF	VDE 1 ms, CQ + QTF CQ, HALO
2.2	DLSF	
2.3	DHSF	VDE 1 ms, QTF TQ, CQ + QTF CQ
2.4	DLSF	
Group 4: Fast VDE (1.55 ms movement to divertor)		
4.1	DHSF, DN	VDE 1.55 ms, CQ + QTF CQ, HALO
4.2	DLSF, DN	
4.3	DHSF', UP	
4.4	DLSF', UP	
4.5	DHSF, DN	VDE 1.55 ms, QTF TQ, CQ + QTF CQ
4.6	DLSF, DN	
4.7	DHSF', UP	
4.8	DLSF', UP	
Group 5: Slow VDE (35 ms movement to PSP, then to divertor in 0.1 ms)		
5.1	DHSF, DN	VDE 35 ms + 0.1 ms, CQ + QTF CQ, HALO
5.2	DLSF, DN	
5.3	DHSF', UP	
5.4	DLSF', UP	
5.5	DHSF, DN	VDE 35 ms + 0.1 ms, QTF TQ, CQ + QTF CQ
5.6	DLSF, DN	
5.7	DHSF', UP	
5.8	DLSF', UP	

The disruption sequences in the particular group are assembled in such a way that the quench of the resultant plasma current at 3 MA/ms rate (CQ) appears after plasma movement. Further, any decrease of toroidal plasma current is accompanied by decrease of the poloidal current (QTF CQ). Effect of thermal quench (QTF TQ) and presence of halo currents are considered exclusively in the proposed list of disruption sequences since they cause poloidal currents in the VV shell in opposite directions and any combination of both should provide lower load on the VV assembly. If halo currents are applied, they appear after the plasma movement when CQ starts.

Currents in the PF and CS coils are kept at constant values for the duration of the disruption sequences in the FE calculations. Toroidal field and initial plasma current are oriented clockwise when viewed from above. Disruption sequences listed in the Table 2 are considered as toroidally symmetrical ones. Spatial distribution of body force density at the time step of the maximal load is used as a boundary condition for the mechanical FE calculation to verify the mechanical design of the VV assembly. Final set of disruption sequences is symmetrical with respect to midplane from the point of view of the electromagnetic FE model; however, it is not the case of the mechanical FE model which is supported only at the bottom lid.

2.3. Asymmetrical disruptions

Noll's formula predicts net lateral force up to 1.7 MN for COMPASS-U parameters and for 20% of plasma current asymmetry:

$$F_x = \pi B_T a_p \delta I_p = 3.14 \cdot 5\ \mathrm{T} \cdot 0.27\ \mathrm{m} \cdot 0.2 \cdot 2\ \mathrm{MA} = 1.7\ \mathrm{MN}$$

Similar value was found running FE model and modelling halo currents injected into the inner column of the VV with the following parameters: I_P = 1.6 MA (pre-disruptive plasma current in the position at inner column), TPF = 2 (toroidal peaking factor), F = 0.375 (halo fraction), B_T = 8.3 T (toroidal field in place of VV inner column), L = 0.72 m (distance between halo strike points along the VV inner column). FE model included the effect of current re-distribution in the VV inner column in the toroidal direction and provided value of approx. 750 kN of net lateral force. Doubling this value should provide safe enough margin for potential dynamic effects, i.e. F_X = 1.5 MN. Scaling based on the JET asymmetrical disruptions suggests that the asymmetrical disruption can last up to 3.26 ms to deliver reasonable force impulse.

For design purposes, net lateral force up to 1.5 MN acting for 3.26 ms was considered as a safe margin.

3. ELECTROMAGNETIC SIMULATIONS

Electromagnetic FE model which was used to calculate EM load of the vacuum vessel was built in the ANSYS Maxwell software [7].

3.1. Comparison of all disruption sequences (5° model of VV)

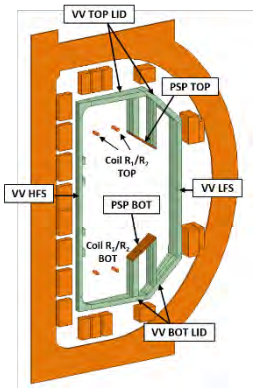

Figure 9: Geometry of 5° model of the VV used for the EM finite element calculation.

Comparison of the critical disruption sequences which are listed in the section 2.2 is done in terms of the maximal force in absolute value (radial, toroidal and vertical component) on the particular parts of the 5° model of the VV sector (Figure 9) observed during the calculated time interval of the disruption event (see Figure 10).

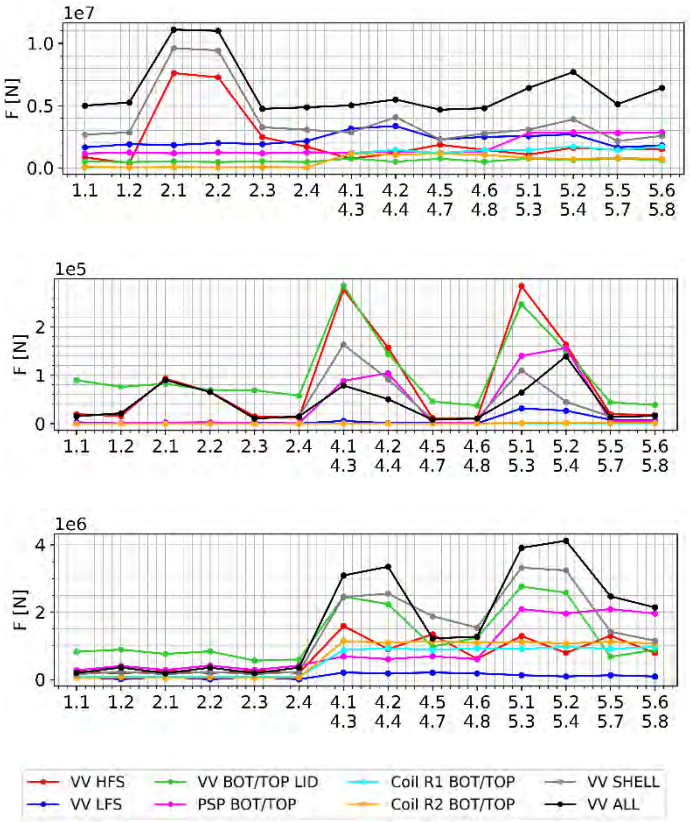

Figure 10: Maxima of the radial, toroidal and vertical force (in absolute value) acting on the particular parts of the FE model for the critical disruption sequences.

Large radial force (7.6 MN) on the VV HFS part is observed for radial disruptions in group no. 2. It is inward force caused by repulsive force from the plasma column at HFS position after the radial movement (–2.5 MN) and by inward force from halo current of about 1.08 MA flowing through the inner VV column which interacts with the toroidal magnetic field (–5.1 MN). Toroidal forces are significantly lower than radial and vertical ones. Maxima of toroidal forces up to 300 kN are observed due to interaction of halo currents with poloidal magnetic field. Large vertical forces (2 MN on top/bottom PSP, 2.7 MN on top/bottom VV lid, 4.1 MN on the whole VV assembly) are calculated for disruption sequences in group no. 5. It is mainly due to the close distance between plasma and PSP after the slow VDE movement and due to halo currents in the bottom/top VV lid interacting with the toroidal field.

Body force density of all of the presented sequences were applied as a load in the subsequent structural analysis. It was shown that disruption sequence no. 5.4 causes the largest mechanical stress in the VV assembly and thus, mechanical design of the VV assembly was mainly verified against this particular loading condition. We provide detailed results of the sequence no. 5.4 calculated on the 45° model of the VV in one of the following paragraphs together with sequence no. 2.2 which loads significantly the inner column of the VV assembly.

3.2. Sequence no. 2.2 (45° model of VV)

Detailed electromagnetic study of the VV assembly was performed using a 45° model of a symmetric VV sector with plasma facing components included. The used geometry and electrical material properties can be viewed in the Figure 11. Disruption sequence no. 2.2 consist of radial plasma movement from the major radius towards the inner column of the VV and consequent current quench accompanied by injection of halo currents into the structure.

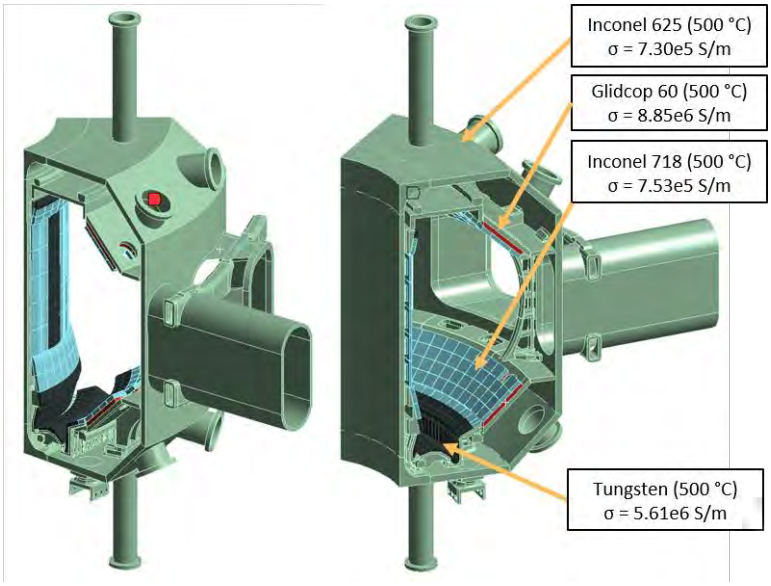

Figure 11: Geometry of a 45° model of a symmetric VV sector with plasma facing components included.

In the Figure 12, current density during the particular disruption phenomena of the sequence no. 2.2 is depicted. VDE + CQ causes toroidal currents, mainly in the inner column of the VV shell and in the conductive parts of the PSP as can be seen also in the Figure 13,

where time evolution of the total induced current (in absolute value) in the particular VV parts is shown. QTF CQ causes poloidal current in the whole VV assembly; however, its value is an order lower compared to the halo current which flows also in the poloidal direction between the strike points of the halo region at inner column of the VV.

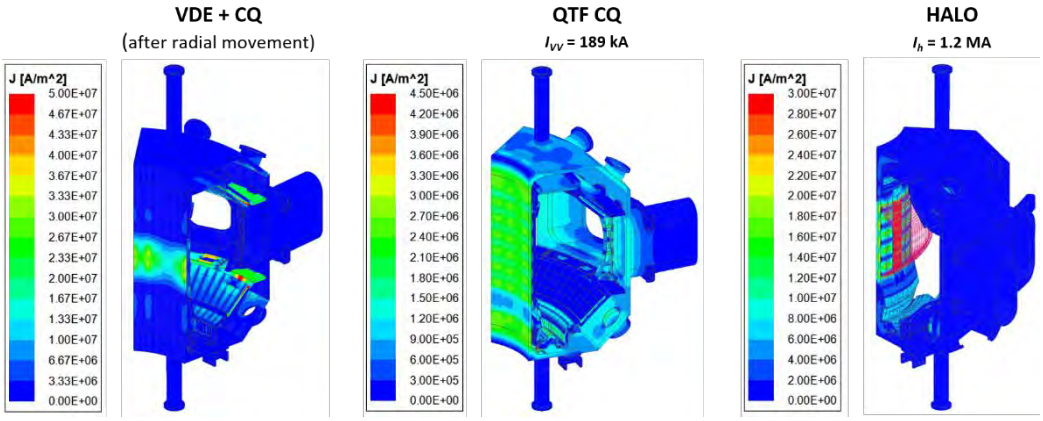

Figure 12: Current density in the VV assembly during disruption sequence no. 2.2.

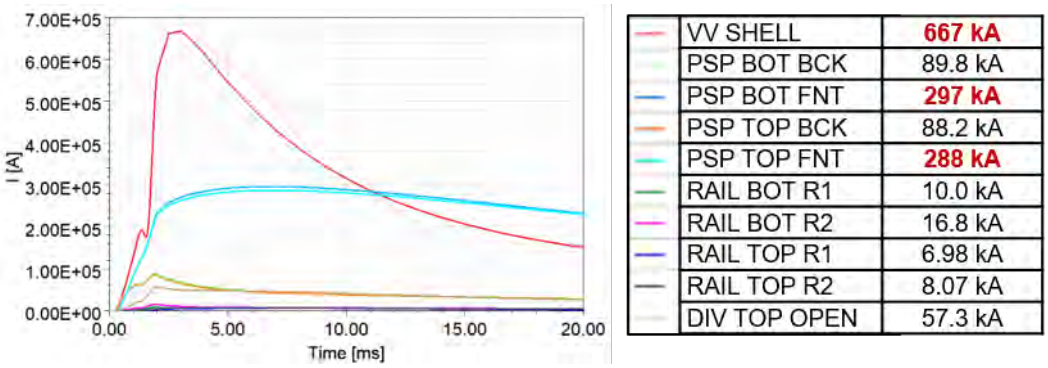

Figure 13: Induced current (in absolute value) in the particular VV parts caused by VDE + CQ events during disruption sequence no. 2.2.

Figures 14 and 15 show resultant forces acting on the respective parts of the VV assembly and on the respective groups of the plasma facing components. It can be seen that very large radial force (up to 7 MN) acts on the inner column of the VV and vertical force up to 0.85 MN acts on the bottom part of the VV. Forces in the toroidal direction are an order lower. Among the PFC groups, significant forces act on the PFC tiles mounted on the inner column (PFC_IWL), upper open divertor (DIV_TOP) and bottom inner divertor baffle (PFC_IDB_BOT).

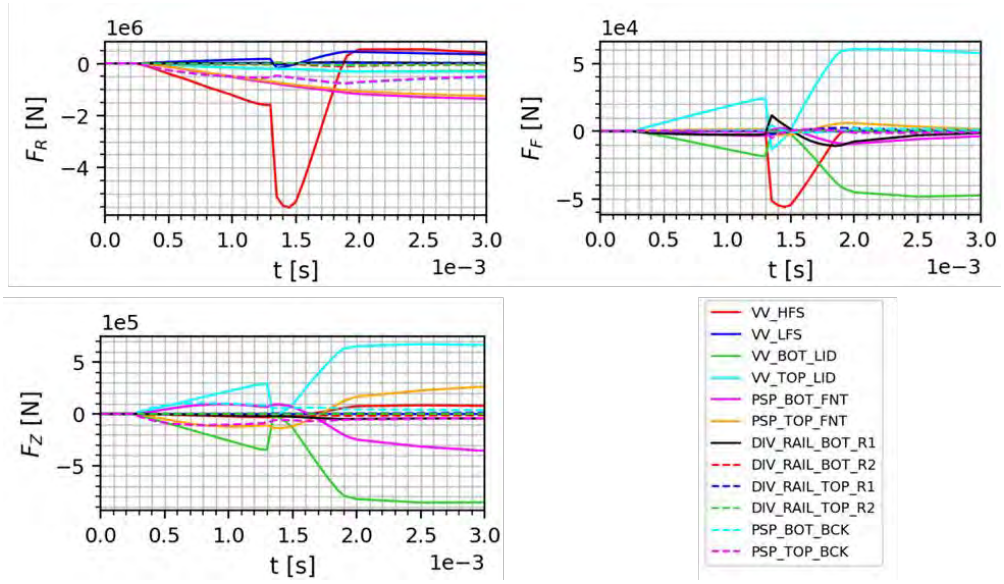

Figure 14: Resultant forces on the particular VV parts during the disruption sequence no. 2.2.

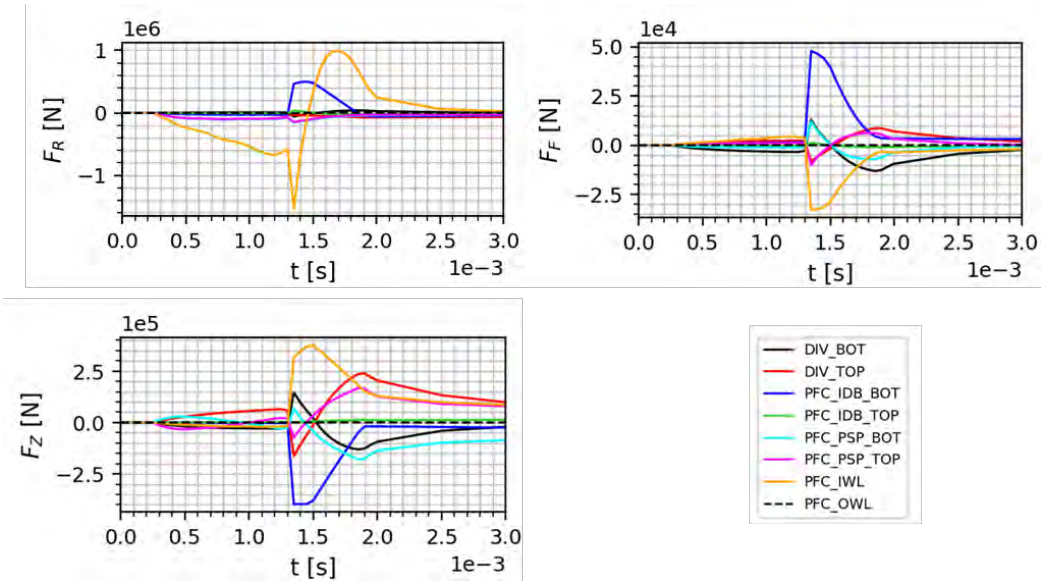

Figure 15: Resultant forces on the respective groups of plasma facing components (PFC) during the disruption sequence no. 2.2.

3.3. Sequence no. 5.4 (45° model of VV)

Sequence no. 5.4 was studied using the same geometry as in the previous paragraph. Disruption sequence no. 5.4 consist of slow plasma movement towards the upper PSP, which then continues by fast movement into the divertor where CQ accompanied by halo currents follow. The same type of figures as in the previous paragraph is used for post-processing of the current case. It can be seen that current density is induced mainly in the upper part of the VV assembly – upper open divertor, upper IDB and PSP and upper lid of the VV shell. The largest forces act exactly on these parts – radial force up to 1.8 MN and vertical force up to 1.2 MN on the upper PSP (PSP_TOP), vertical force up to 2.2 MN on the upper open divertor (DIV_TOP), radial force up to 1.2 MN on the upper IDB (PFC_IDB_TOP) and radial force 2 MN on the PFC tiles which are mounted on the upper PSP (PFC_PSP_TOP).

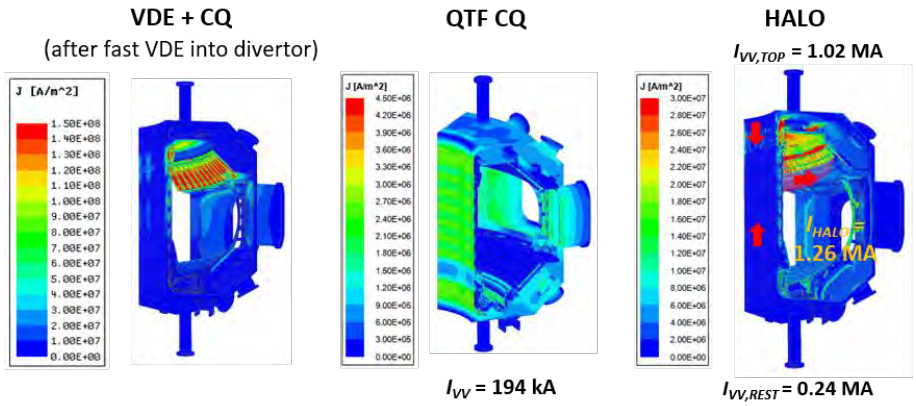

Figure 16: Current density in the VV assembly during disruption sequence no. 5.4.

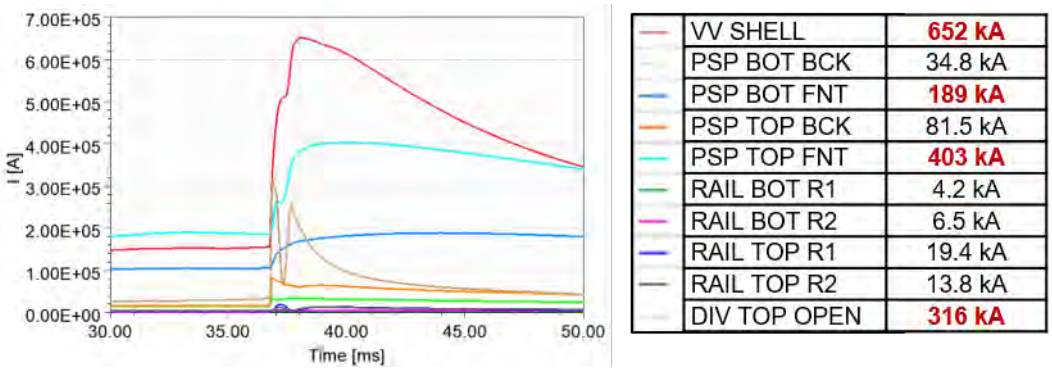

Figure 17: Induced current (in absolute value) in the particular VV parts caused by VDE + CQ events during disruption sequence no. 5.4.

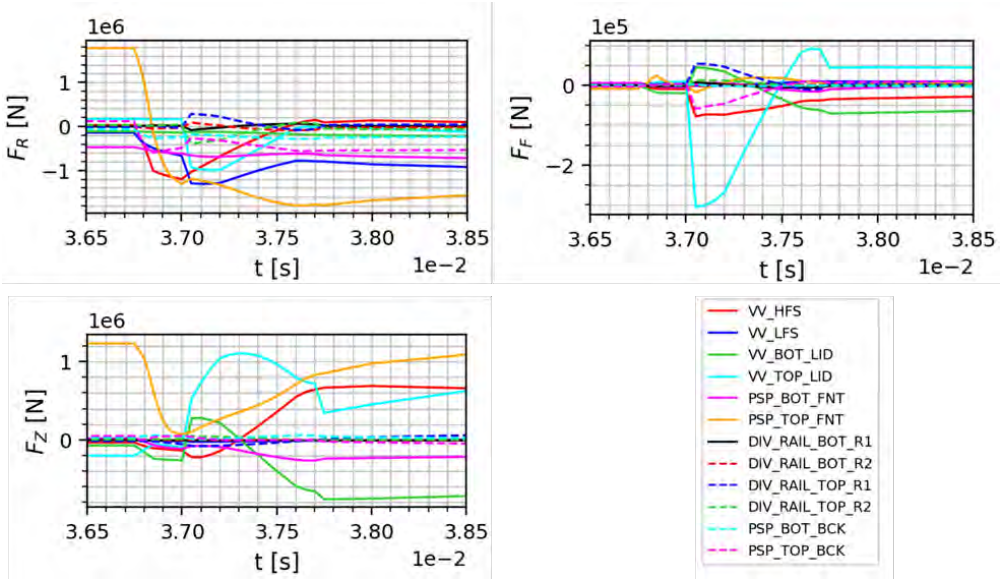

Figure 18: Resultant forces on the particular VV parts during the disruption sequence no. 5.4.

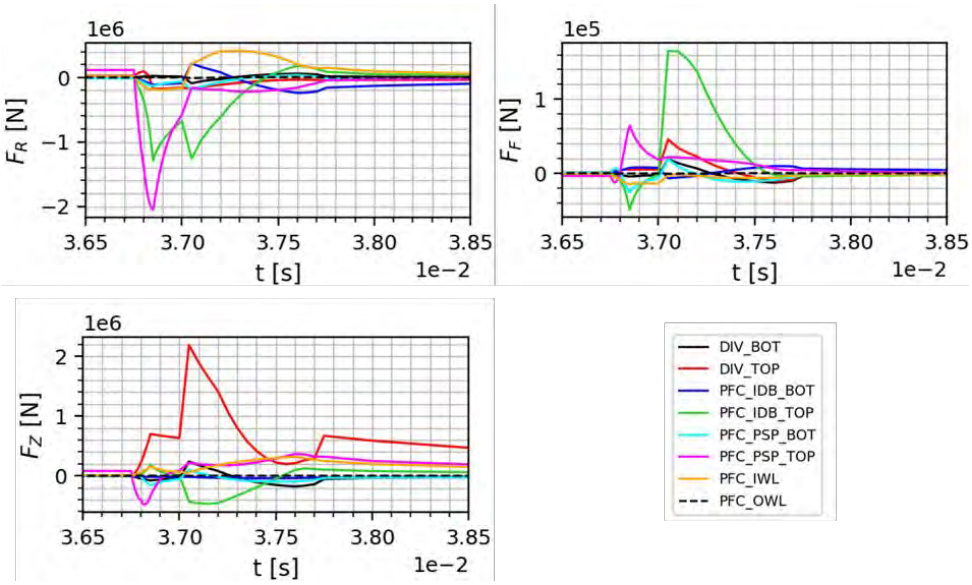

Figure 19: Resultant forces on the respective groups of plasma facing components (PFC) during the disruption sequence no. 5.4.

4. HEATING SIMULATIONS

As described in the technical specification, the vacuum vessel will be heated up by heating system. Heating will be provided by gaseous medium (preferably CO2, Helium or Argon), flowing through welded-on tubular channels.

To ensure temperature homogeneity, several simulations were run.

4.1. Simple (1/16) heating model

To review preliminary stresses in vacuum vessel, simple model was constructed. Features:

- Geometry
  - 1/16 of vacuum vessel
  - Inner PFCs simplified
- Pipes model
  - Heating channels modelled as 1D approximation.
- Boundary conditions
  - All contacts bonded
  - Inlet temperature increasing from RT to 500 °C within 24 hours
  - Port ends temperature fixed @RT
  - Leg ends temperature fixed @80 K
  - Outer vessel surface enabled with radiative heat transfer

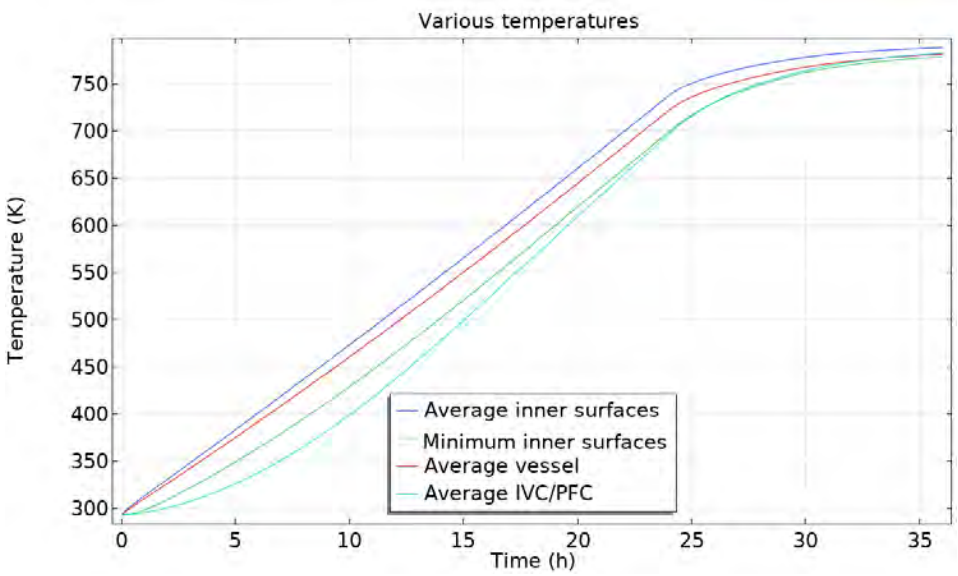

Figure 20: Resulting temperatures [K]

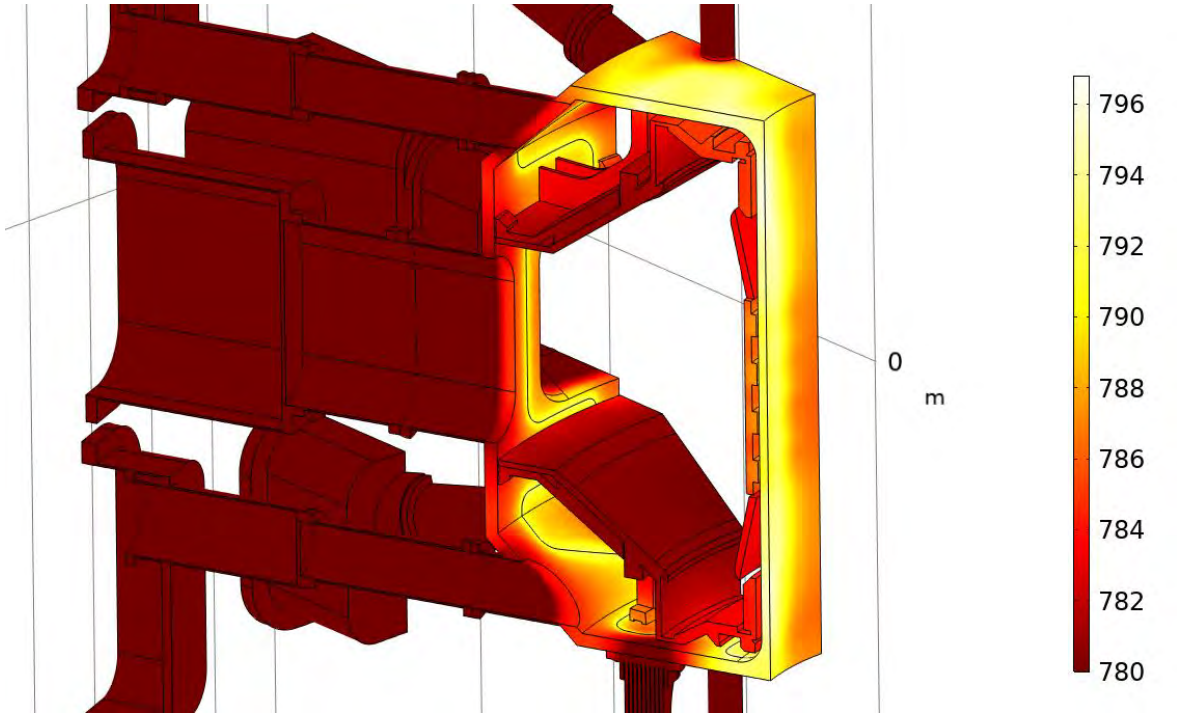

Figure 21: Temperature [K] distribution at the end of heating

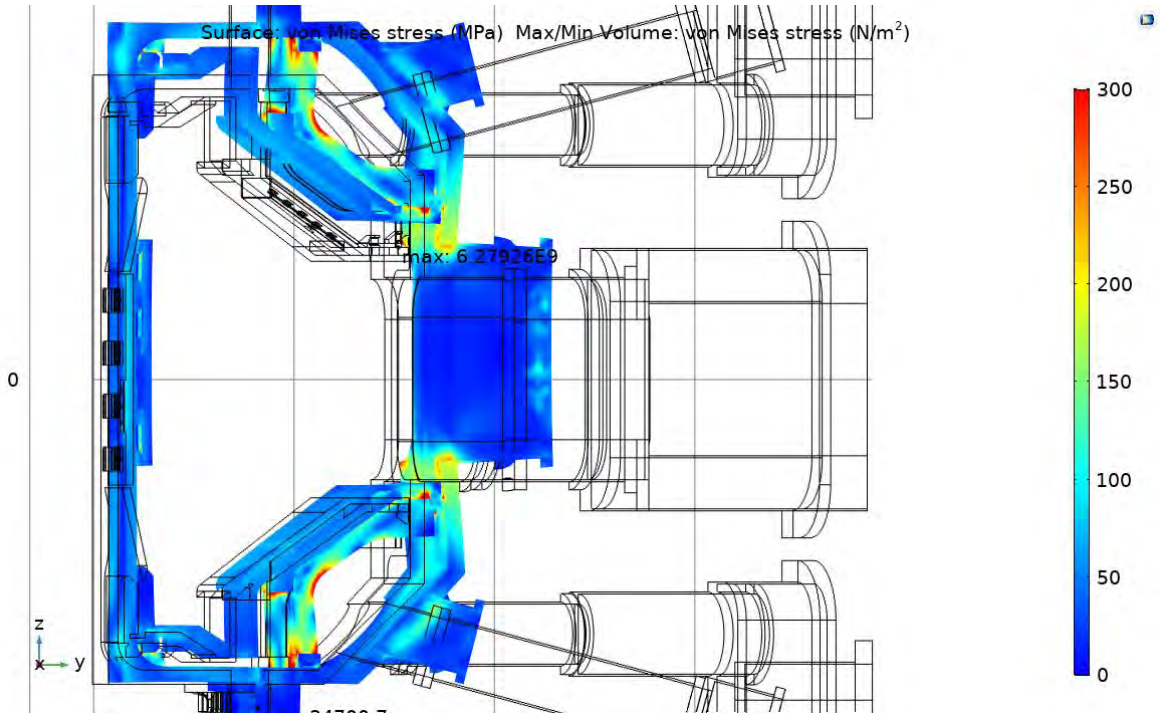

Figure 22: Stress [MPa]distribution at T=15 h

4.2. Complex all-machine global thermal mode

As the COMPASS-U is a complicated machine with a small dimensional footprint and high component concentration, it was necessary to assess the thermal situation in the whole COMPASS-U assembly – thermal radiation between all parts is an important factor and cannot be neglected as in model described in section 4.1.

Global thermal model features are:

- Geometry
  - 1/8 of whole tokamak assembly
  - Full resolution components: vacuum vessel (VV), support structure (SS), cryostat
  - Simplified components: PF coils, TF coils, plasma-facing components
- Pipes model
  - Heating channels of VV modelled as 1D approximation
  - Cooling channels of SS modelled as 1D approximation.
- Boundary conditions
  - All contacts bonded
  - Port ends temperature fixed @RT
  - Leg ends temperature fixed @80 K
  - Radiative heat transfer both in vessel and out of vessel
- Inlet temperatures
  - Cooling of support structure within first 7 days
  - Heating up vacuum vessel between 7-9 day
    - First day heating up, second day thermalization

RESULTS:

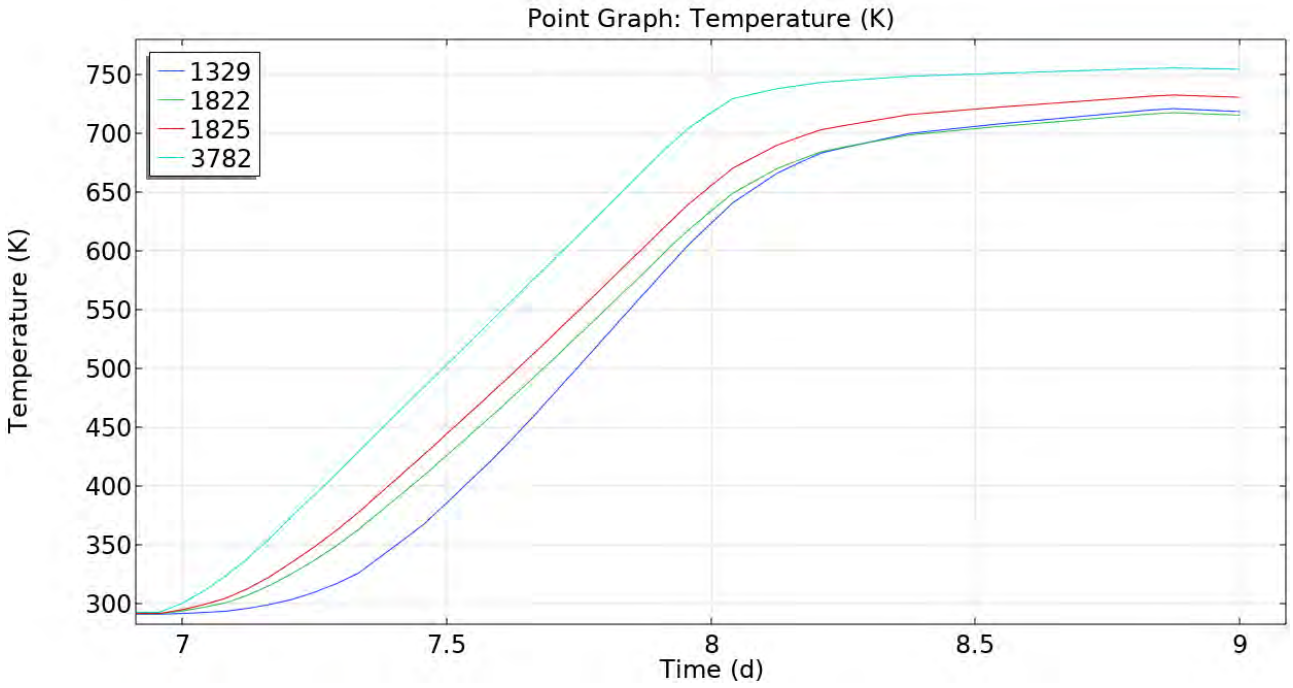

Figure 23a: Temperatures [K] at different points of vacuum vessel

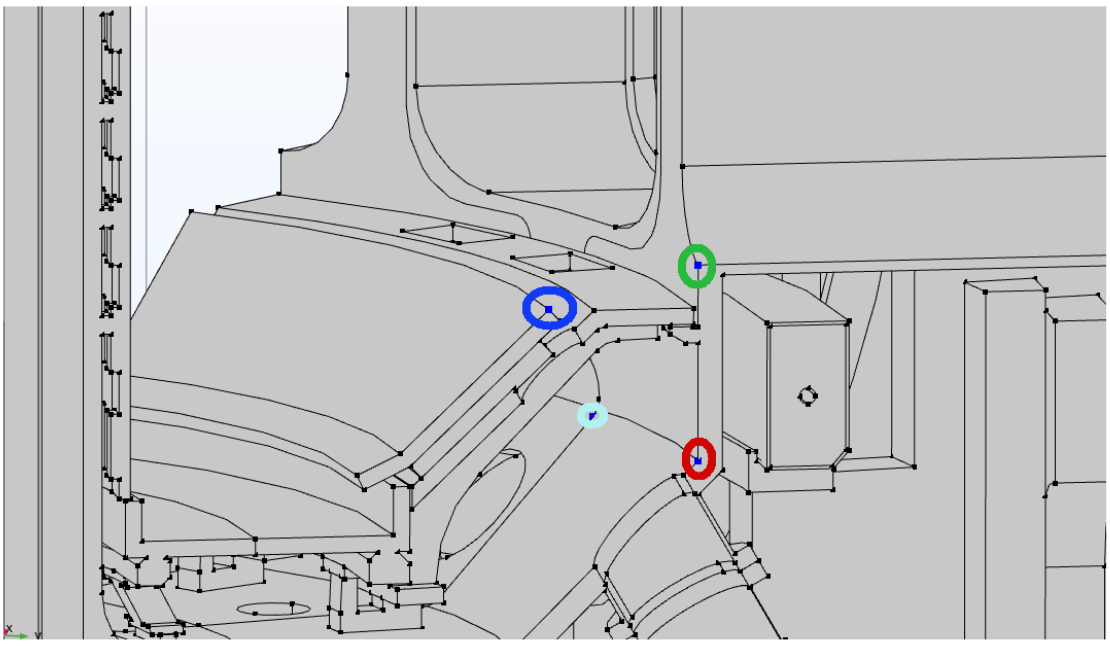

Figure 23b: Temperatures [K] at different points of vacuum vessel

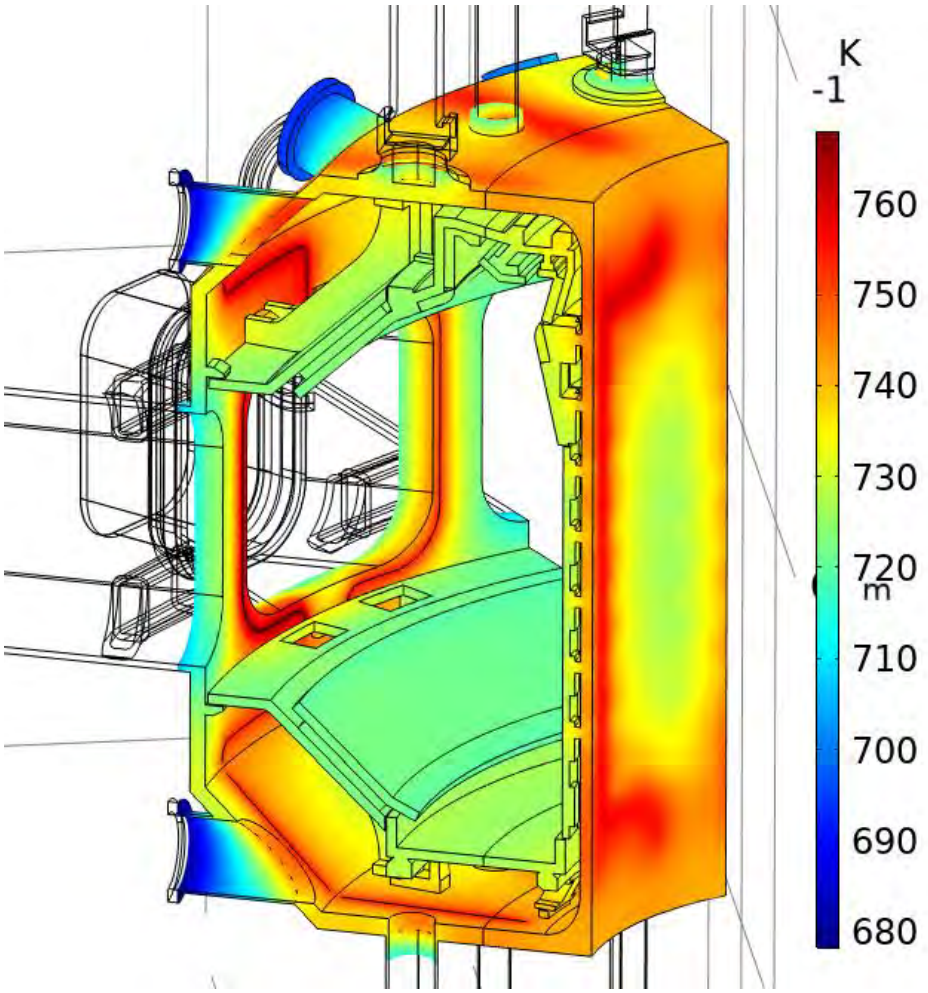

Figure 24: Temperature distribution [K] in the VV at the end of the heating (t = 9 days)

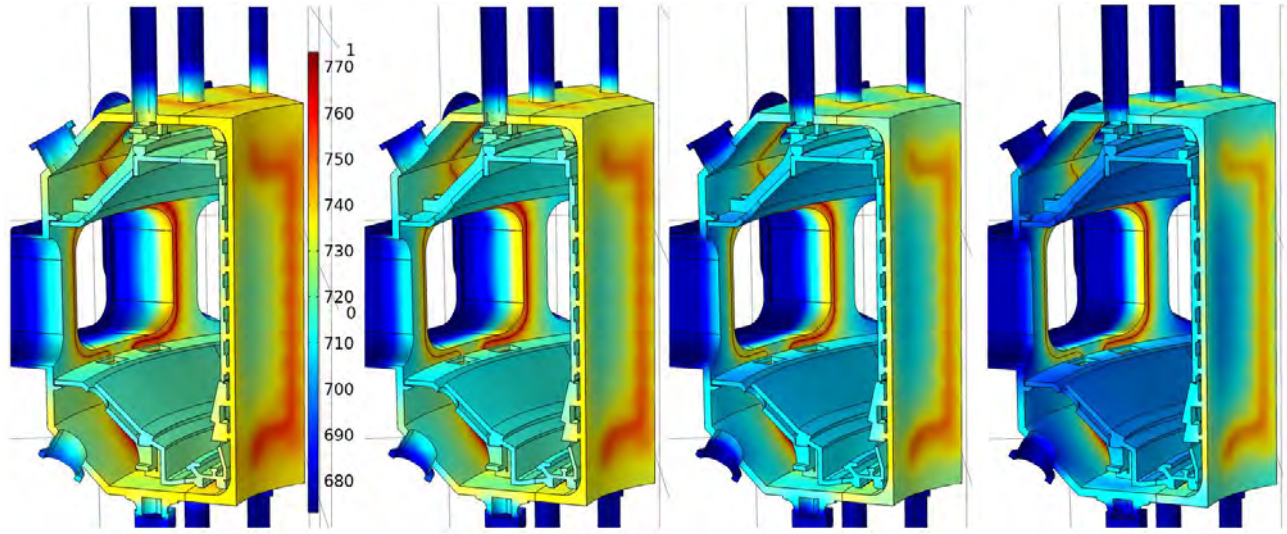

Figure 25: Comparison of VV temperature [K] with different insulations (ε = 0.005, 0.01, 0.02, 0.03)

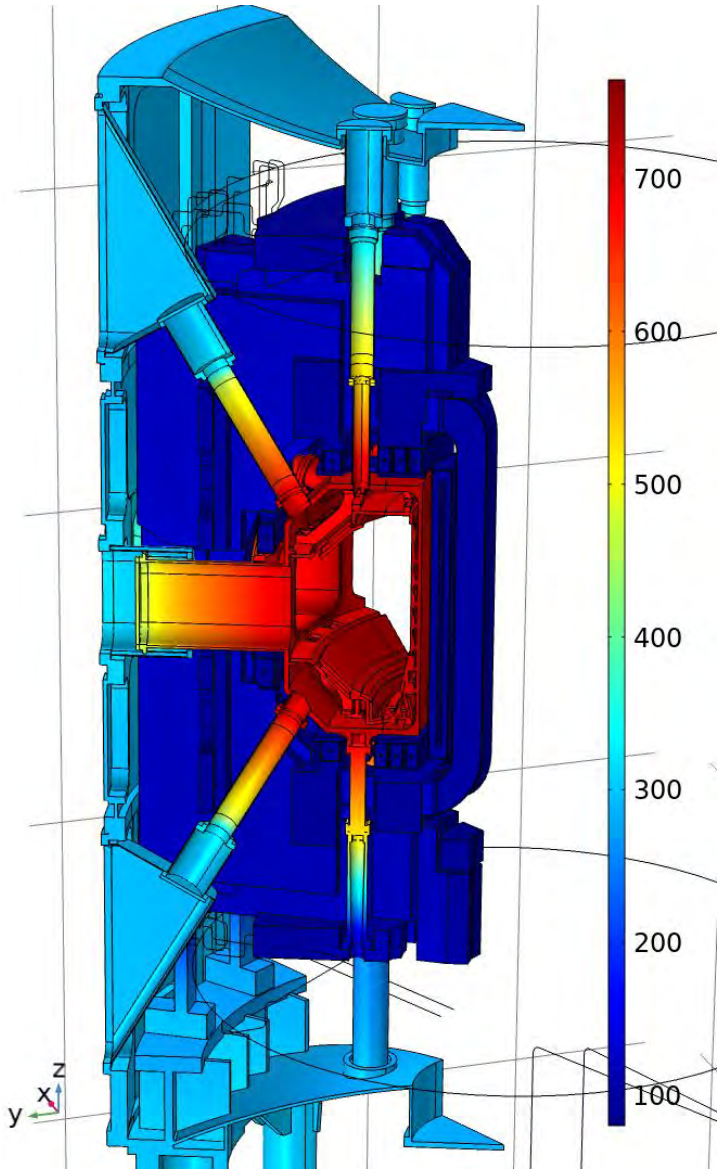

Figure 26: Temperature [K] map of whole global thermal model.

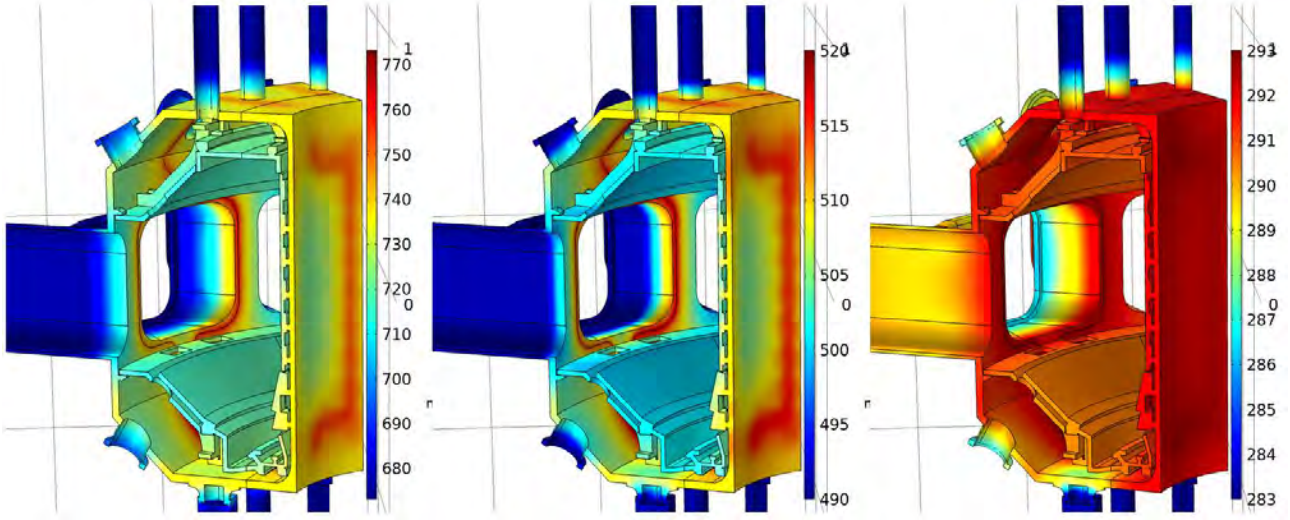

Figure 27: VV temperature [K] distributions for 3 different heating scenarios (500 °C, 250 °C, RT]

5. STRUCTURAL ANALYSES

In this section the results of key structural analyses are presented. Loading scenarios used are in accordance to scenarios described in chapter 2 and 3. In general, for structural analyses the loading scenario no. 5.4 was used (see chapter 3.3).

Note that here presented results cover continuous development of the vacuum vessel and include some out of date designs and results. These results should serve as a general overview of individual high loaded areas and expected stresses or issues.

5.1. Vacuum Vessel deformations

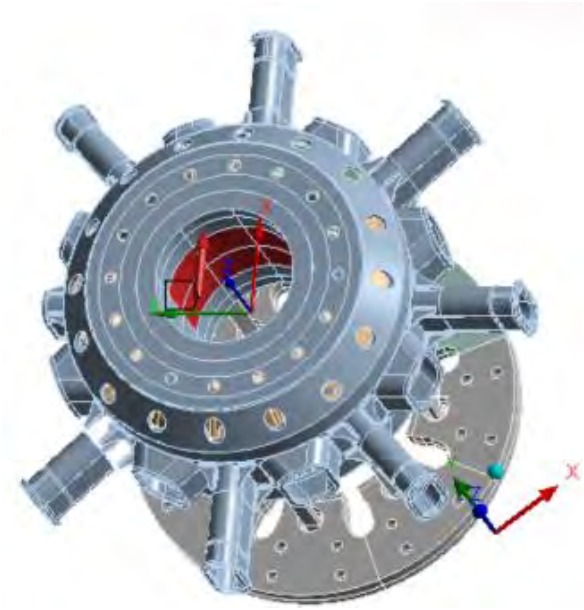

Figure 28: FEM model setup

Loading: Earth gravity & Thermal & Fz- & Lateral Force Impulse

Free MN ports
Max. over time
21.8 mm

Toroidal fixing at MN ports
Max. over time
18.4 mm

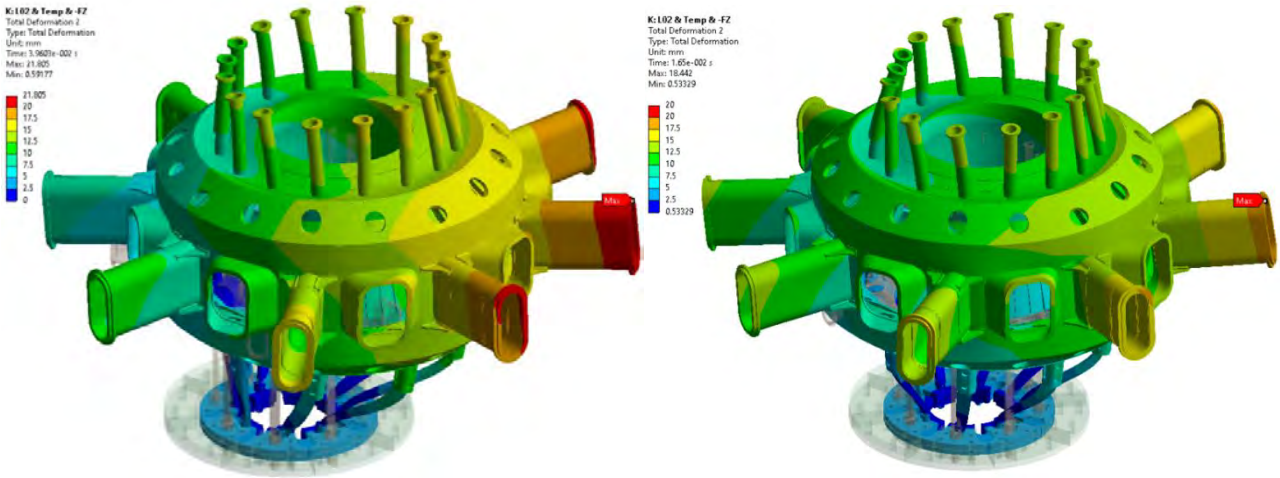

Figure 29: Maximum deformations of the VV depending on fixation of the MN ports, negative vertical force

Loading: Earth gravity & Thermal & Fz+ & Lateral Force Impulse

Free MN ports
Max. over time
22.9 mm

Toroidal fixing at MN ports
Max. over time
24.8 mm

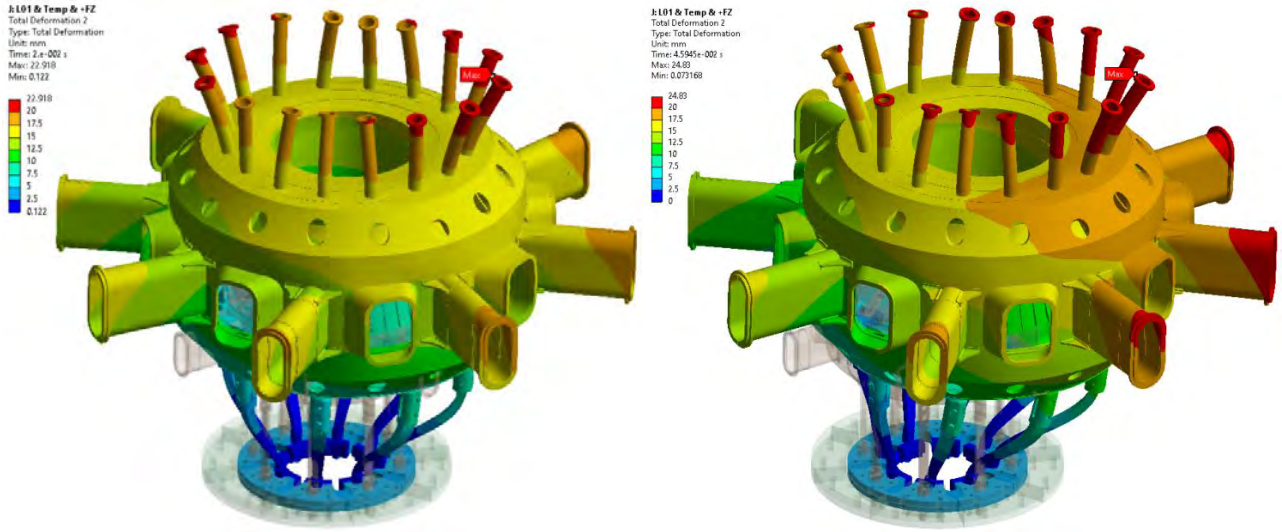

Figure 30: Maximum deformations of the VV depending on fixation of the MN ports, positive vertical force

Conclusion: The fixing at the MN ports does not help very much.

5.2. High field side analysis (not up-to-date design)

Loading: scenario 5.4a

Max. over time
260 MPa

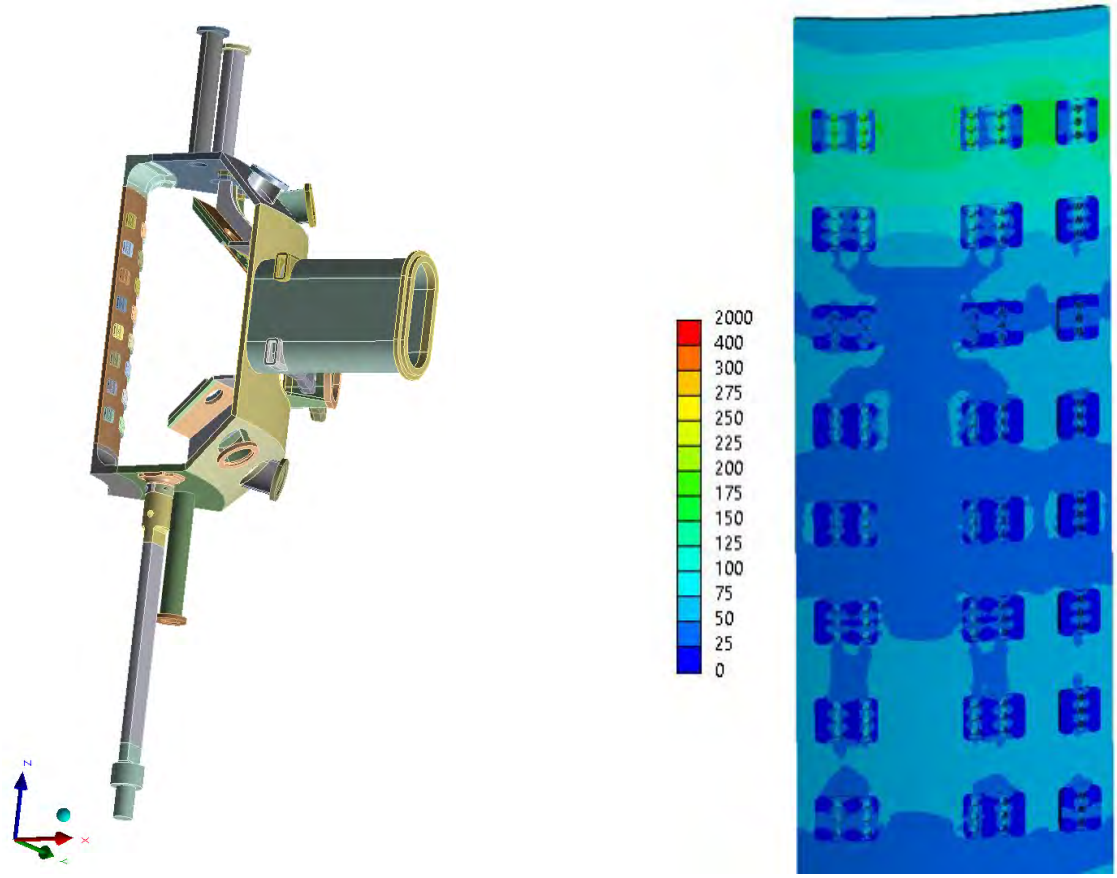

Figure 31: Stresses in the area of the high field side

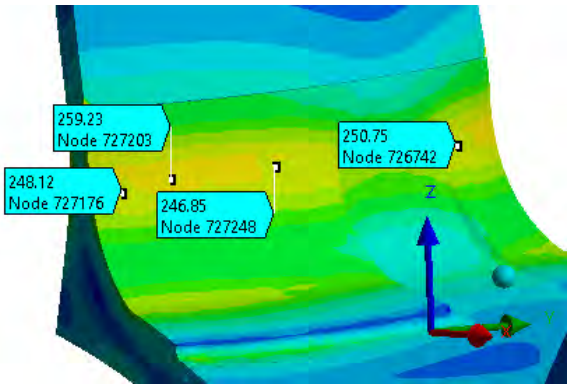

Figure 32: Stresses in the area of the forged ring

Conclusion:

- The stresses are fully acceptable for HFS pads
- Increased stresses occurred in the VV bottom corner as expected

5.3. Low Field Side Analysis

Loading: Bolt pretension + 500 °C + Electromagnetic forces (scenario 5.4a)

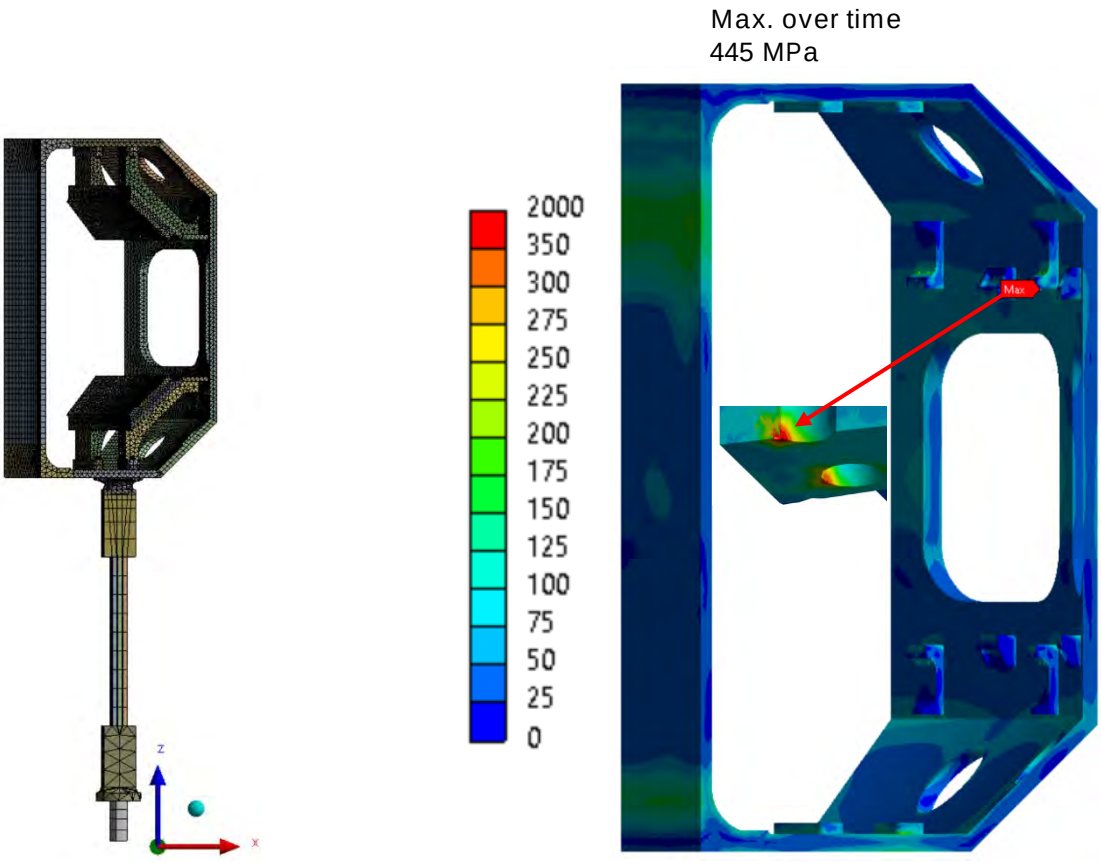

Figure 33: Stresses in the area of the low field side

Conclusion:

- In general, the LFS pads design is OK but local preloading in M14 thread could occur
- Some bolts are overloaded

- Torque box connection to pad in lids shall be redesigned either by changing the load path and/or increase M12 screw radius (main stress contribution is due to thermal loading)
- Torque box connection to LFS pad through the torque box plate shall be redesigned or at least fatigue check shall be performed
- Torque box connection to LFS pad through OHP could withstand the loading considered but fatigue check is recommended

5.4. Vacuum Vessel Support Legs

Loading: Earth gravity & Thermal gradient (-200 (bottom) ÷ +500C (top)) & Static Vertical Force & Lateral Force Impulse

Figure 34: FEM model setup

Max. over time
578 MPa
(Top adaptor radius)

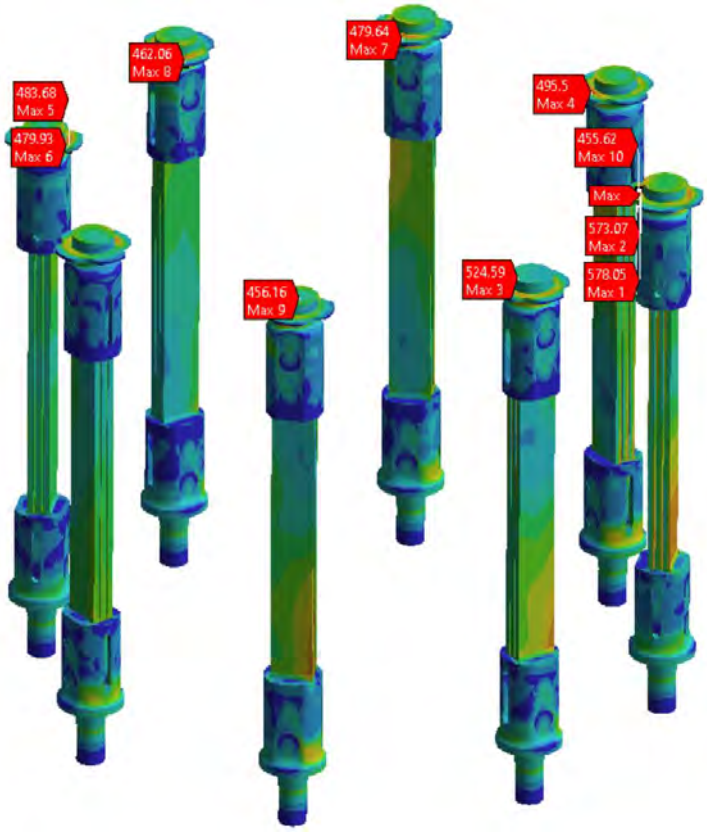

Figure 35: Stresses in the VV supports

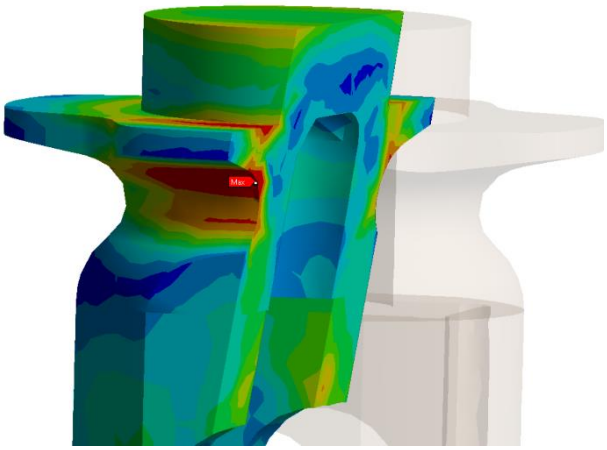

Figure 36: Stresses in the VV support upper adaptor

Conclusion:

- Increased stresses in upper adaptor radius
- Excessive stresses if the upper adaptor is welded along its side to the VV bottom lid (not shown in the figure)

5.5. Vacuum Vessel Body

Loading: Earth gravity & Thermal gradient (-200 (bottom) to +500C (top)) & Static Vertical Force & Lateral Force Impulse

Figure 37: FEM model setup

Max. over time
578 Mpa
(Top adaptor radius)

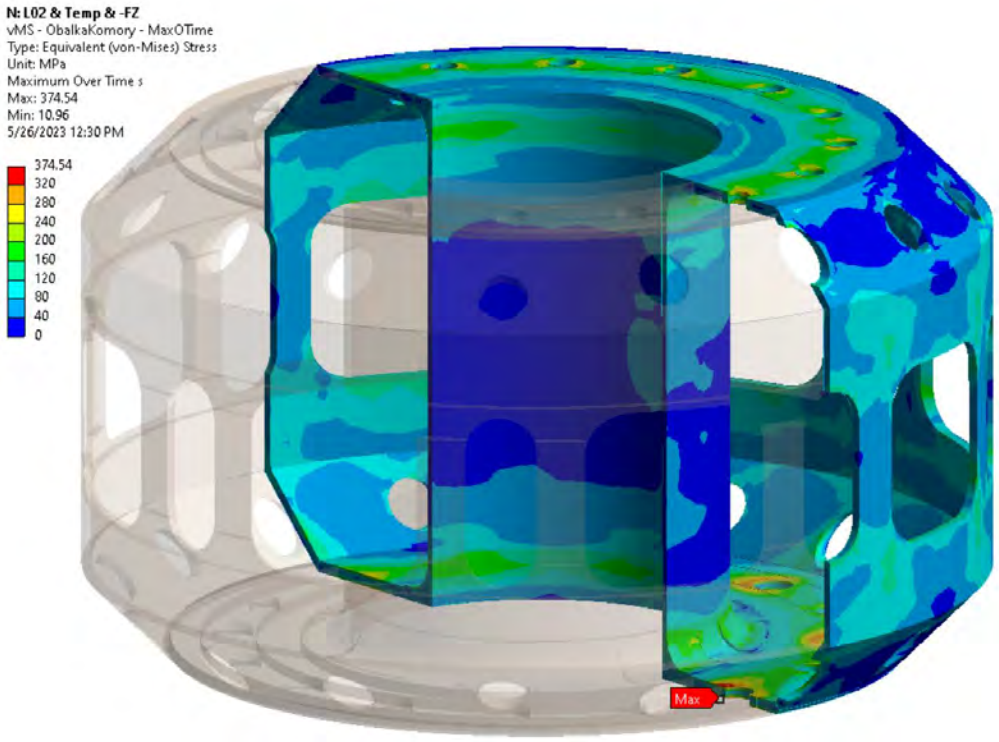

Figure 35: Stresses in the VV body

5.6. Thermal Expansion

Temperature distribution

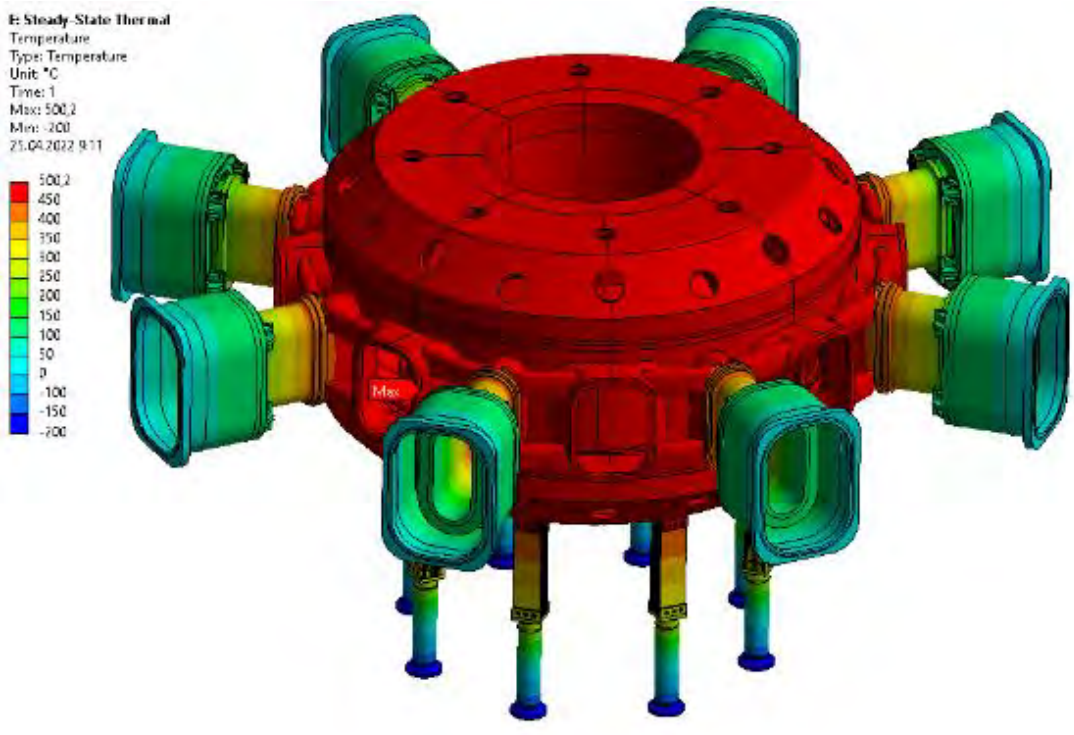

Figure 35: Temperature distribution in the VV assembly

Port type/ Reference surface	Maximum radial deviation (mm)	Maximum vertical deviation (mm)
MX1	6,315	12.718
MX2	6,311	3.654
MN1	8,583	12.442
MN2	8,582	3.557
DIV DUX	8.783	12.18
DIV DLX	8.781	4.631
DIV DUC	8.783	12.18
DIV DLC	8.781	4.631
DIV DUH	8.783	12.18
DIV DLH	8.781	4.631
VU	10.514	9.406
VL	10.520	6.675
1	3,676	13.248
2	3,655	3.109
3	9.332	10.579
4	9.335	5.471

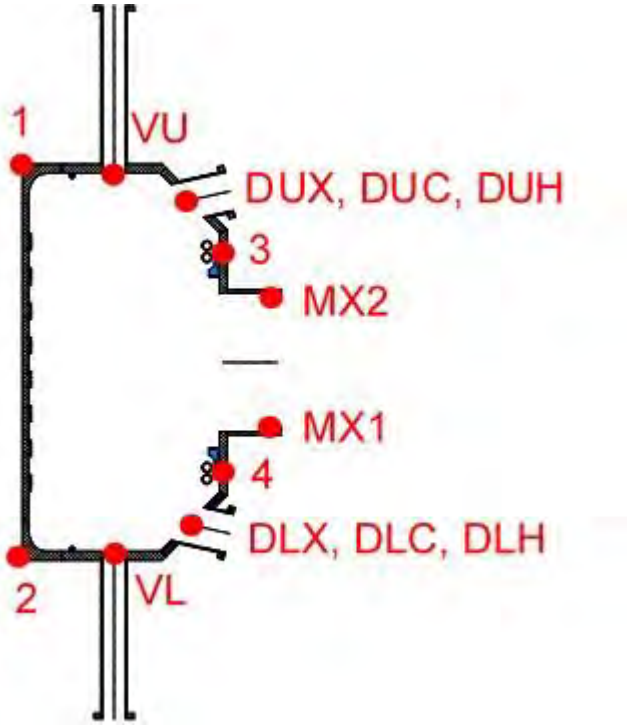

Table 3: Stresses in the VV body

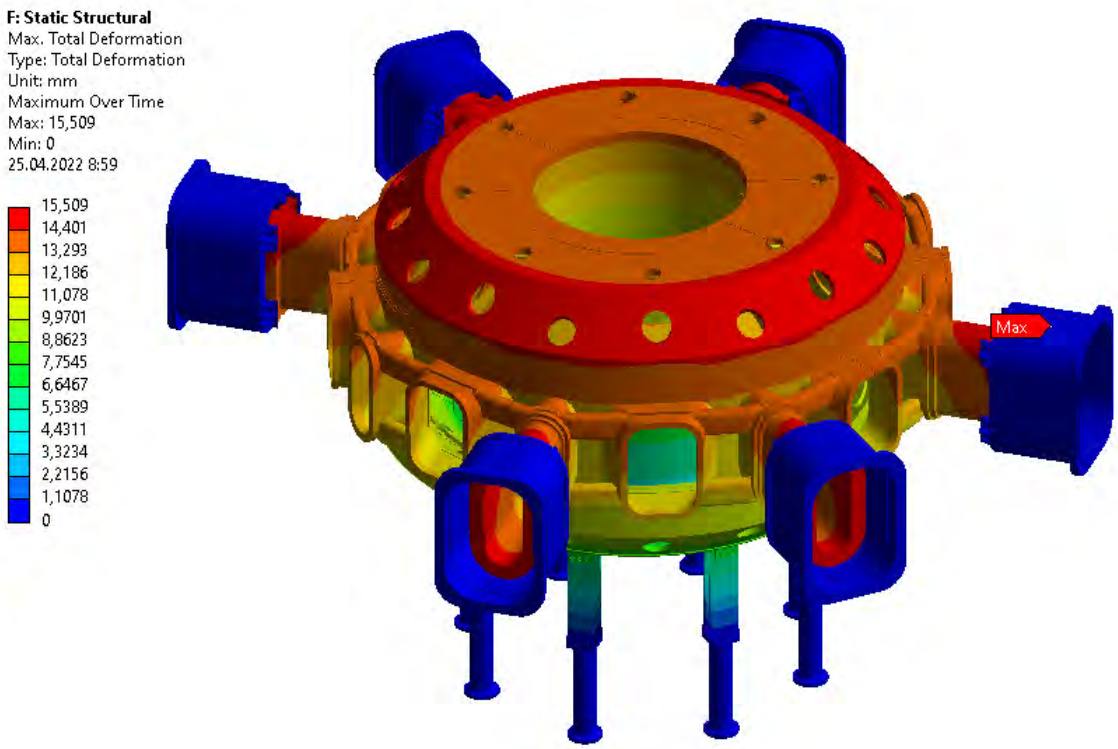

Figure 36: Total deformation of the VV assembly under heat load

5.7. Modal Analysis

5.7.1. FEM 45 deg

Mode 1
Global Toroidal mode
10.1Hz

Mode 2
Global Vertical mode
79.5Hz

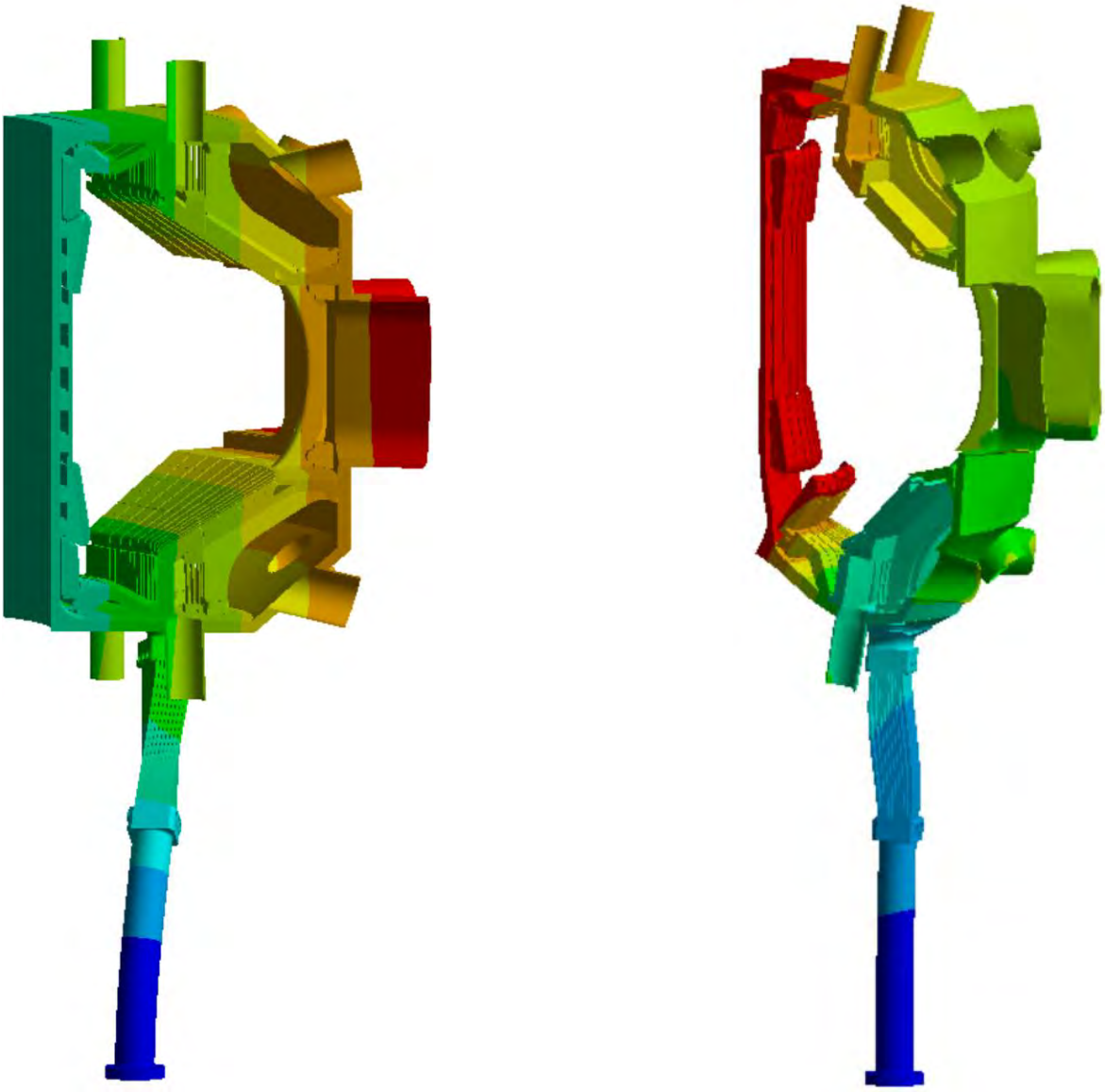

Figure 37: Total displacement of the VV at defined frequencies

5.7.2. FEM 360 deg

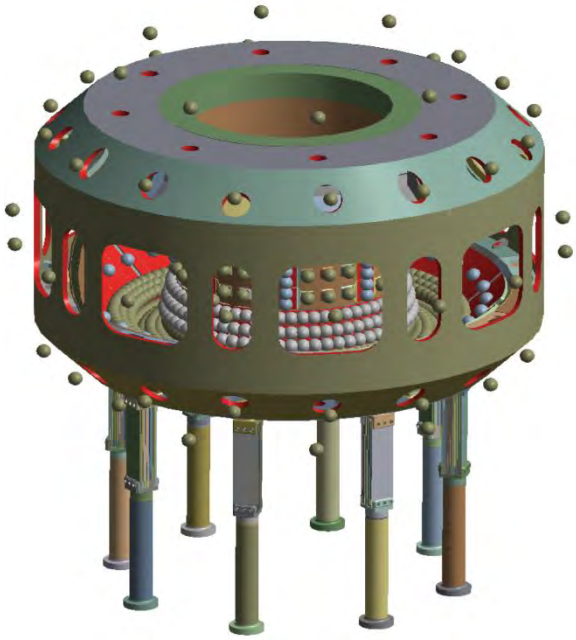

50 modes were calculated

EFFECTIVE MASSES

Effective masses greater than 5.0% of total rigid mass are displayed

N	Freq(Hz)	Mxx(t)	Myy(t)	Mzz(t)	Ixx(kg.m^2)	Iyy(kg.m^2)	Izz(kg.m^2)
1	27.4	0.06	0.01		0.01	0.06	
2	34.2	0.01	0.06		0.07	0.01	0.06
3	123.7	0.02			0.01	0.05	
5	218.9		0.01		0.05	0.01	0.01
15	480.5	0.01				0.02	
25	569.3			0.09	0.01	0.06	
34	745.4		0.01		0.02		0.01
36	864.3					0.02	

EFFECTIVE MASSES FRACTIONS

1	27.4	48.9%	7.9%		3.8%	18.5%	
2	34.2	8.9%	55.6%		28.9%	3.6%	64.3%
3	123.7	16.7%	2.7%		3.1%	15.3%	
5	218.9	2.1%	13.0%		19.1%	2.4%	15.1%
15	480.5	4.85%	0.76%		1.27%	6.32%	
25	569.3			76.23%	3.97%	19.54%	
34	745.4	0.77%	4.71%		8.23%	1.02%	5.54%
36	864.3	3.77%	0.62%		1.10%	5.28%	
M eff cumulative		0.10	0.10	0.09	0.17	0.22	0.08
		86.42%	87.06%	77.47%	72.77%	72.86%	87.17%
M residual		0.02	0.01	0.03	0.06	0.08	0.01
M rigid		0.11	0.11	0.11	0.24	0.30	0.09

Figure 38: 360 deg model setup

Mode 1
7.5 Hz
1st global horizontal mode
mainly in y-axis
(see the effective masses fraction)

Mode 2
7.5 Hz
1st global horizontal mode
mainly in x-axis
(see the effective masses fraction)

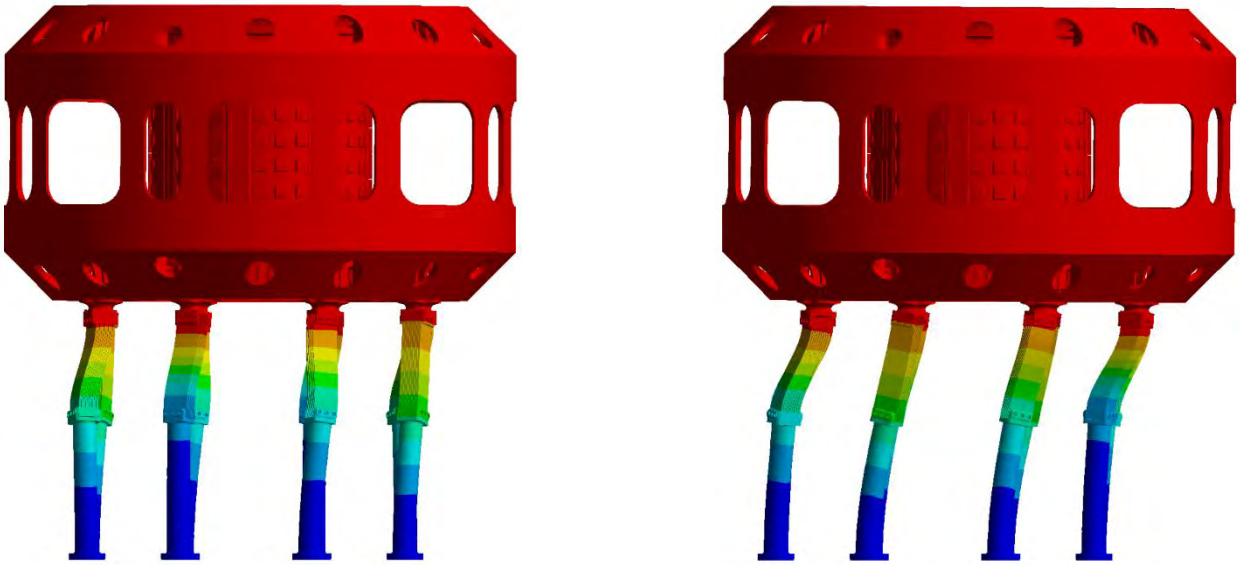

Figure 39: Total displacement ofs the VV at defined frequencies

Mode 3
12.1 Hz
1st global toroidal mode

Mode 4
52.7 Hz
1st global bending mode
mode around x-axis
(see the effective masses fraction)

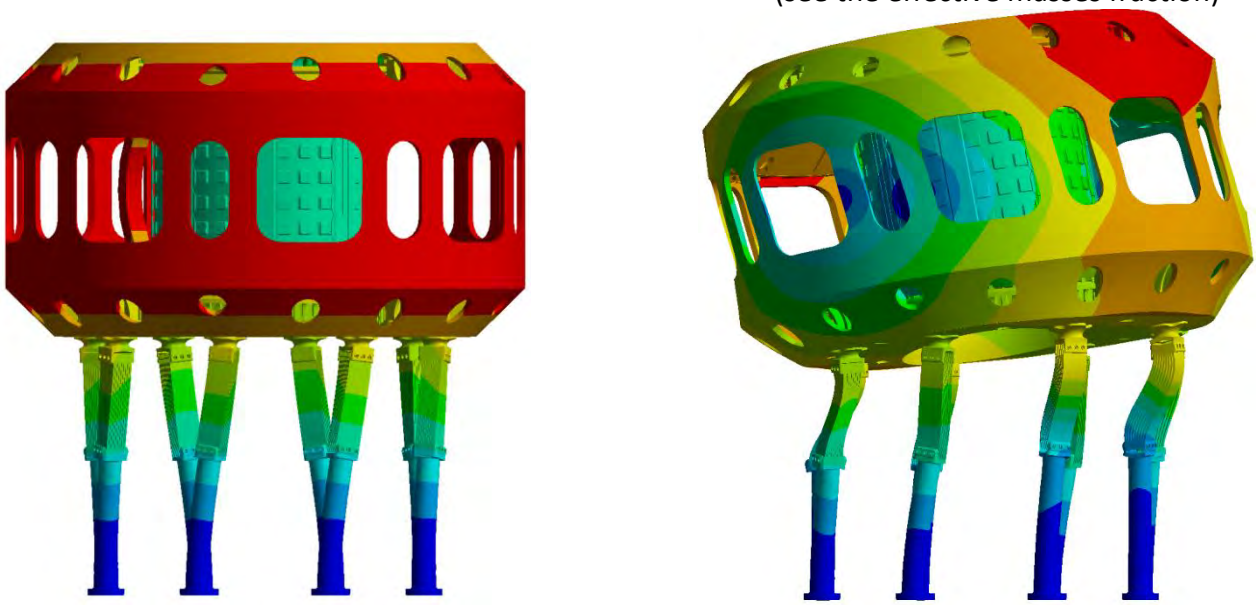

Figure 40: Total displacement of the VV at defined frequencies

Mode 5
52.8 Hz
1st global cross bending mode
mode around y-axis
(see the effective masses fraction)

Mode 6
75.6Hz
first global vertical mode

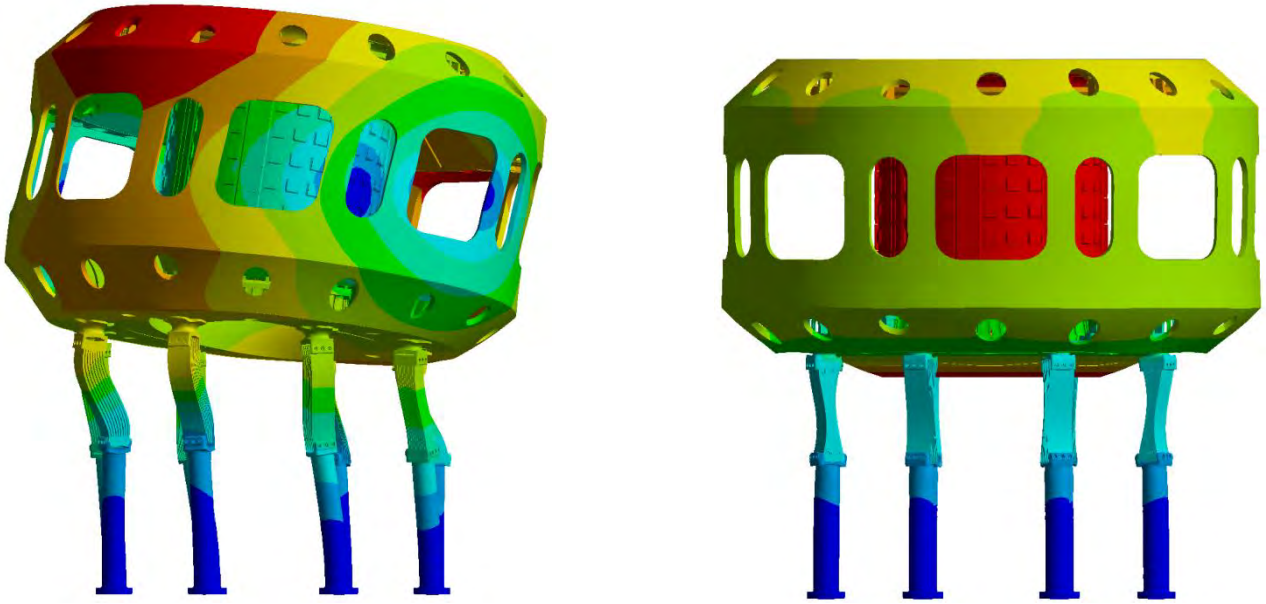

Figure 41: Total displacement of the VV at defined frequencies

5.8. Overpressure analysis

Loading: Outer pressure 0.1 MPa, application to the pink areas

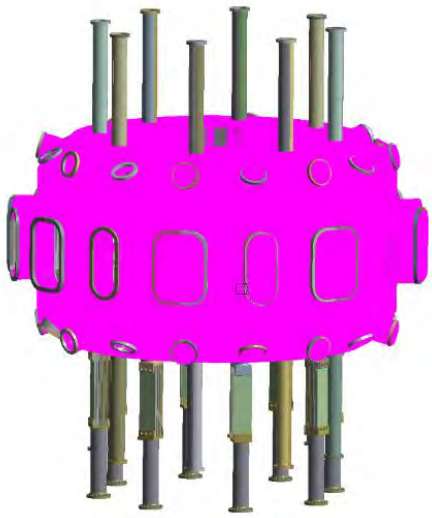

Figure 42: FEM model setup

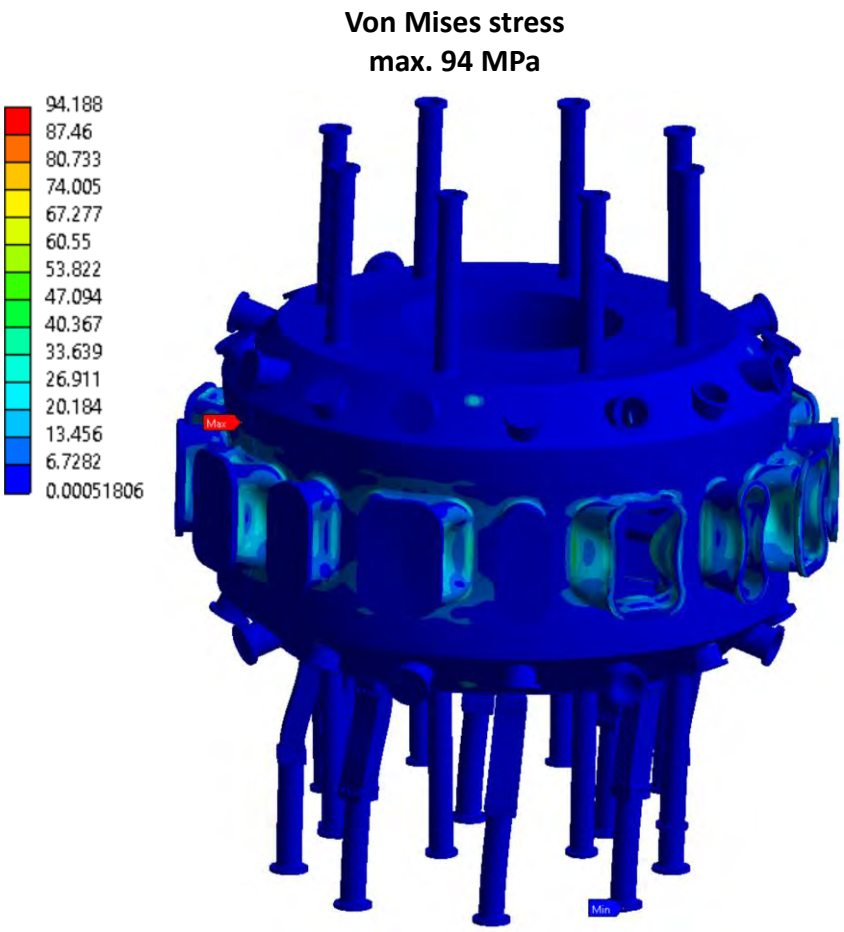

Figure 43: Stresses in the VV at defined pressure load

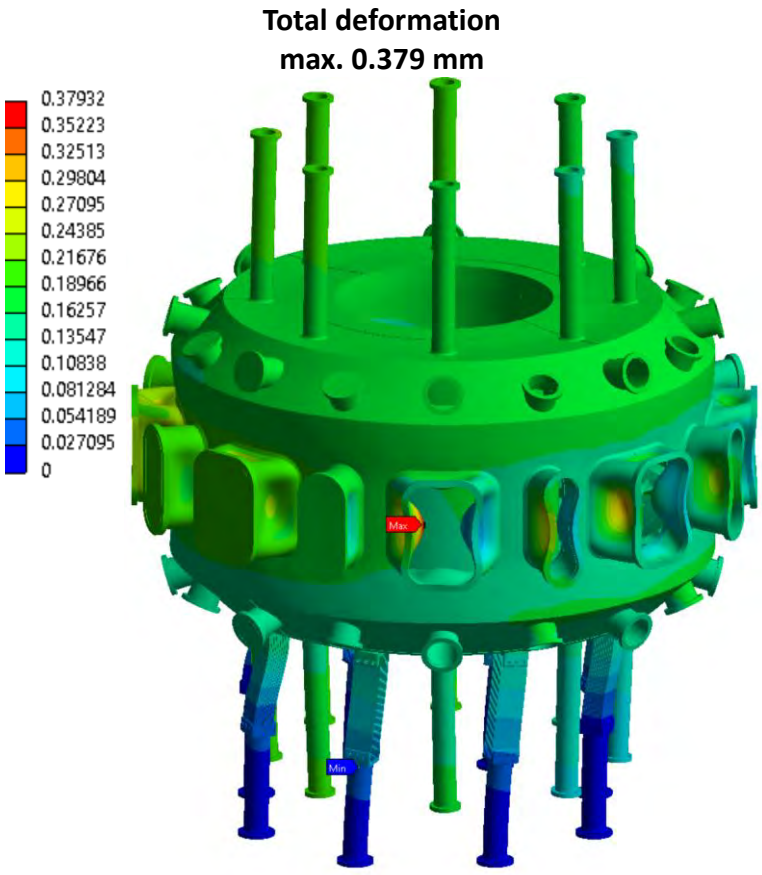

Figure 44: Total deformation of the VV at defined pressure load

6. REFERENCES

[1] J. C. Wesley et al., Disruption Characterization and Database Activities for ITER, Proceedings of the 21st IAEA Fusion Energy Conference, China, 2006, IT/P1-21.

[2] T. C. Hender et al., ITER Physics Basis, Chapter 3: MHD stability, operational limits and disruptions, Nuclear Fusion 47 (2007) S128-S202.

[3] G. Cunningham, High performance plasma vertical position control system for upgraded MAST, Fusion Engineering and Design 88 (2013) 3238-3247.

[4] J. F. Artaud et al., Metis: a fast-integrated tokamak modelling tool for scenario design, Nuclear Fusion 59 (2018) 105001.

[5] V. D. Pustovitov, Disruption-induced poloidal currents in the tokamak wall, Fusion Engineering and Design 117 (2017) 1 – 7.

[6] ITER Physics Expert Group on Disruptions, Plasma Control and MHD and ITER Physics Basis Editors, Chapter 3: MHD stability, operational limits and disruptions, Nuclear Fusion 39 (1999) 2251-2389.

[7] ANSYS® Academic Research Maxwell, Release 2019 R3 – 2022 R1.